Journal of Materials Research and Technology 38 (2025) 2408–2422

Contents lists available at ScienceDirect

Journal of Materials Research and Technology

journal homepage: www.elsevier.com/locate/jmrt

Synergistic microstructure refinement and enhanced mechanical properties in hypoeutectic Al–Si-based alloys via high-entropy microstructure refiner

Jae Kwon Kim [a], Yagnesh Shadangi [a,b], Min Seok Kim [a], Myeong Jun Lee [a], Eun Soo Park [a,*]

[a] Department of Materials Science and Engineering, Research Institute of Advanced Materials & Institute of Engineering Research, Seoul National University, Seoul, 08826, Republic of Korea

[b] Department of Materials Science and Metallurgical Engineering, Indian Institute of Technology Bhilai, Durg, 491001, Chhatishgarh, India

ARTICLE INFO

Keywords:
Hypoeutectic Al–Si alloy
High-entropy microstructure refiner
Synergistic multiphase refinement
Mechanical property
Streamlined post-process

ABSTRACT

As the demand for lightweight and energy efficiency in Al–Si-based alloys continues to grow, the T5 heat treatment is increasingly preferred instead of T6, owing to its streamlined processing and reduced susceptibility to product distortion. Nevertheless, T5 treatment presents challenges in managing coarse α-Al dendritic structures and eutectic Si phases. Although commercial refiners like Al–Ti–B and Sr are used for microstructural refinement, there is a critical need for more effective refiners for multi-phase manipulation. Herein, we report a novel high-entropy microstructure refiner (HMR) that enables synergistic microstructure refinement under T5 heat treatment for hypoeutectic Al–Si alloys. In particular, the $(TiZrNb)_2(CrFeNi)$ HMR, which combines Group A elements (Ti, Zr, Nb) to decrease ΔT_N (nucleation undercooling, quantitatively validated by DSC) by forming heterogeneous nucleation sites and Group B elements (Cr, Fe, Ni) to induce ΔT_C (constitutional undercooling) through segregation at the liquid/solid interface (verified through EPMA), achieves synergistic multi-phase microstructure refinement. This refinement simultaneously reduces the size of α-Al dendrites (to about one-tenth), secondary dendrite arm spacing (by about half), and eutectic Si spacing (by about half) while maintaining low intermetallic compound precipitation, compared to hypoeutectic Al–Si base alloy. This synergistic microstructure refinement simultaneously increases both yield strength (and ultimate tensile strength) and elongation, thus overcoming the typical trade-off among these properties. We believe that the results of this study provide an effective guideline for the development of cast (or T5-treated) aluminum alloys based on the application of novel HMRs, resulting in a cost-effective, streamlined post-process.

1. Introduction

The hypoeutectic Al–Si–Mg alloys have gained significant prominence in the automotive, aerospace, and structural materials industries due to their excellent castability, specific strength, and corrosion resistance [1–3]. Al–Si–Mg alloys are widely recognized for their suitability for T6 heat treatment, a process that enables these alloys to achieve their maximum mechanical properties [4]. The solution treatment of T6 heat treatment, which is conducted at relatively high temperatures (~540 °C), generally involves water-quenching to achieve supersaturation and homogenization of solutes [5]. However, this can cause distortion in the final products [6]. Recently, T5 heat treatment, which omits the solution treatment, has sometimes been preferred over T6 heat treatment due to the benefits of part integration for product light-weighting and energy savings, which are becoming increasingly important [7]. Nevertheless, applying this process is challenging since the solution treatment is not performed, meaning that the coarse casting microstructure, including α-Al dendrites, eutectic Si structures, and numerous intermetallic compounds formed during solidification, remains in the final product [8,9]. Xu et al. reported in several studies that such microstructures can be significantly refined under rapid solidification and high undercooling conditions through dendrite remelting and stress-induced recrystallization [10–13]. These mechanisms are known to play a major role in grain refinement under non-equilibrium solidification conditions. However, due to the stringent processing conditions and issues with reproducibility, applying these mechanisms in commercial productions remains challenging. Therefore, a detailed investigation into the addition of grain-refining elements, which are known to

* Corresponding author.
E-mail address: espark@snu.ac.kr (E.S. Park).

https://doi.org/10.1016/j.jmrt.2025.08.039
Received 29 April 2025; Received in revised form 4 August 2025; Accepted 6 August 2025
Available online 6 August 2025

be the most effective method for achieving a fine-grained microstructure, is becoming increasingly important [2]. In hypoeutectic Al–Si alloys, grain refiners are roughly divided into two roles depending on the target microstructure. The first role of grain refiners is to refine the columnar structure composed of α-Al dendrites, while the second role is to modify the morphology and size of the eutectic Si [14]. The Al–Ti or Al–Ti–B systems, including Al–5Ti–1B, Al–3Ti–1B, and Al-2.5Ti-2.5B, along with other variations in Ti and B proportions, are commonly utilized for the first role [15–21]. When these grain refiners are added to the aluminum melt, they promote the development of numerous substrates that serve as potential sites for heterogeneous nucleation during the solidification of aluminum alloys [22]. Although aluminide (Al_3Ti), formed through the addition of a Ti refiner, actually acts as a strong heterogeneous nucleation site via edge-to-edge matching—which refers to the formation of a crystallographic relationship where specific atomic planes of two different phases interlock with each other—it has a misfit of less than 10 % with Al [23]. However, it is difficult to achieve significant grain refinement effects due to poor phase stability at pouring temperatures (680°C-730 °C) and high solubility (e.g., >0.15 wt% Ti) in Al melts [24]. Additionally, when Ti and B are added together, TiB_2 and Al_3Ti can easily form. TiB_2 remains highly stable even at high temperatures above 2500 °C and has very low solubility in liquid Al, which allows for the formation of a large number of initial nuclei. $TiAl_3$ surrounds the TiB_2 surface and significantly reduces the lattice misfit between TiB_2 and α-Al (from 4.22 % to 0.09 %). This substantial reduction in misfit enhances the potential for the nucleation of α-Al [25]. However, when more than 5 wt% Si is added, as is common in casting Al–Si alloys, the grain refinement performance of Al–Ti or Al–Ti–B refiners noticeably decreases. This is due to the well-known Si-poisoning effect. A common explanation for the Si-poisoning effect is the formation of different bulk silicides on the surface of TiB_2, which not only hinders the nucleation of α-Al but also reduces the growth restriction by utilizing solute Ti [26]. Therefore, recent studies have actively focused on developing new α-Al dendrite grain refiners, such as Al–Zr, Al–Nb, Al–Ti–Nb–B, and Al–Ti–B–C, to minimize the Si-poisoning effect and achieve superior grain refinement performance [17,27–30]. Among the candidate grain-refining elements, Ti, Zr, and Nb are particularly effective due to their ability to form aluminide phases (Al_3Ti, Al_3Zr, and Al_3Nb) that exhibit favorable edge-to-edge crystallographic matching with the α-Al matrix [15,23,27,28]. These compounds possess lattice misfits within 10 %, enabling them to serve as potent heterogeneous nucleation sites. Notably, the addition of Nb has also been shown to alleviate the detrimental Si-poisoning effect that impairs α-Al dendrite refinement. This improvement is attributed to the enhanced high-temperature phase stability of the resulting aluminide compounds. For modifying eutectic Si structures, elements such as Na, Sb, and Sr are commonly utilized for the second role of refinement. Among these elements, Sr is widely used in the form of master alloys and is known for its excellent grain refinement effects, making it the most commonly used grain refiner. The refinement mechanism of Sr for modifying the shape and controlling the size of eutectic Si is well known, including the restricted twin plane re-entrant edge (TPRE) and impurity-induced twinning (IIT). Both mechanisms are based on twinning reactions promoted by Sr atoms present in the Liquid (*L*)/Solid (*S*) coexistence region [31]. However, alkaline earth metals like Sr are expensive as raw materials and have a low vaporization temperature (boiling point 1377 °C), making them very difficult to process [2]. Furthermore, the refinement effect of Sr saturates at a certain eutectic Si size, and the effectiveness decreases with excessive addition due to the formation of coarse Al–Si–Sr intermetallic compounds [32]. Moreover, precise control of Sr content for optimal refinement of eutectic Si is very difficult due to its low evapLi/oration temperature (boiling point, 1377 °C. To achieve more effective eutectic Si refinement and lower production costs, alternative candidate alloying elements are required. Recently, research has been conducted on refining the eutectic Si phase by adding relatively inexpensive transition metals such as Cr, Fe, and Ni, which are expected to segregate at the Liquid-Solid (L/S) interface and induce similar mechanisms [33–35]. The alloying elements conventionally assigned to the two refinement tasks Ti + B for α-Al dendrite refinement and Sr (or Na, Sb) for eutectic-Si modification differ sharply in solubility, vapor pressure, reaction kinetics, and thermal stability. Each element therefore requires its own optimal addition temperature, holding time, and melt chemistry. Attempting to satisfy these mutually incompatible processing windows in a single casting operation greatly increases cycle time, raises costs, and undermines process stability, making independent control of the two element groups impractical at an industrial scale. Meanwhile, Zhang et al. [36] reported that the addition of an AlCoCrFeNiTi high-entropy alloy (HEA) based refiner to pure aluminum enhanced the efficiency of α-Al dendrite refinement and improved mechanical properties. However, studies reporting the application of HEA-based refiners to Al–Si alloy systems with more complex microstructures remain extremely limited.

From the above, the current Al–Si alloy industry demands enhanced efficiency from commercial refiners and cost reduction through process simplification. Therefore, in this study, we develop a novel high-entropy microstructure refiner (HMR), $(TiZrNb)_2(CrFeNi)$, which is capable of simultaneously refining the α-Al dendritic structure, secondary dendrite arm spacing, and eutectic Si spacing with a simplified manufacturing and dosing process. We focused on demonstrating the synergistic multiphase microstructure refinement effects of the developed HMR through microstructural and mechanical property evaluations.

2. Experimental

Silafont®-36 (AlSi10MnMg, Rheinfelden), fabricated by Daiki Aluminum Industry, was used as the base alloy (hereafter BA) in this study. To ensure consistency in the casting and cooling process, the Silafont-36 ingots were re-melted using Arc Plasma Melting (APM) under a Ti-gettered high-purity argon atmosphere (Arc melting and suction casting system, SAMHAN VACUUM). The $(TiZrNb)_{100-x}(CrFeNi)_x$ (x = 0, 33, 50, 66, 100 at%) refiners (hereafter HMR) were fabricated by APM under the same Ti-gettered high-purity argon atmosphere. The purities of the elements used were Ti (99.995 %), Cr (99.95 %), Fe (99.98 %), Ni (99.99 %), Zr (99.95 %), and Nb (99.95 %). The HMRs after crushing were melted with BA respectively using APM to fabricate the five different (BA+0.5 wt% HMR) alloys. The BA + HMR ingots were re-melted at least six times to ensure good chemical homogeneity and rectangular specimens (14 mm width × 6 mm thickness × 50 mm height) were produced by copper mold drop-casting under an argon atmosphere. The cast alloys were annealed at 200 °C for 1 h (artificial aging of T5 heat treatment) in an air atmosphere and subsequently quenched in water. The software Thermo-Calc was used to simulate the Scheil solidification and predict the binary phase diagram of Al-X (X being the added elements). The simulations were conducted using the SSOL6 and TCBIN thermodynamic databases to assess phase stability.

Phase identification was confirmed by X-ray diffraction (XRD; D2 Phaser, Bruker) using Cu-Kα (λ = 1.5418 Å) radiation. The 2θ range was scanned from 20° to 80° with a scanning rate of 0.02° per second to achieve high intensity. High-energy synchrotron XRD was performed to obtain more accurate phase analysis information at the P21.1 beam line of the Deutsches Elektronen-Synchrotron (DESY, Germany). The wavelength of the X-ray beam was 0.1222 Å. Diffraction patterns were obtained in transmission mode by using a 2D PerkinElmer amorphous silicon detector with 2048 x 2048 pixels and pixel size of 200 x 200 μ m^2. Each diffraction pattern was acquired with a total exposure time of 5 s, divided into 5 sub-frames of 1-s exposure each to prevent saturation of the detector. The microstructure of the annealed sample was confirmed using Field-emission Scanning Electron Microscopy (FE-SEM; Amber X, TESCAN) with Secondary Electron (SE), Energy Dispersive X-ray Spectroscopy (EDS), Backscattered Electron (BSE), and Electron Backscatter Diffraction (EBSD; QuantaX, BRUKER) modes. To qualitative and quantitative analysis of trace elements the Electron Probe Micro

Analysis (EPMA) was performed using the JEOL JXA-IHP 200F operating at a voltage of 20 keV, Pixels 256 x 192 and a dwell time of 100 ms. The specimens used for analyzing the material characteristics were prepared from the identical locations within the rectangular samples and were polished to achieve a mirror-finish surface condition.

The heat flow curves were measured by Thermogravimetric Analysis/Differential Scanning Calorimetry (TGA/DSC; METTLER TOLEDO) to identify variations in thermal characteristics. Measurements were conducted from 25 °C to 750 °C with a heating rate of 5 °C/min to 40 °C/min (5, 10, 20 and 40 °C/min) in a high-purity argon atmosphere. To ensure complete melting under all compositional conditions, the samples were overheated by approximately 160 °C above the melting point of the Al-10.3 wt% Si binary composition (590 °C) and held for 10 min.

The mechanical properties were confirmed by uniaxial tensile test (Instron 5967, INSTRON, Norwood, USA) at an engineering strain rate of 10^{-3}/s. Rectangular dog-bone-shaped specimens for the uniaxial tensile test were machined from the annealed samples using Electrical Discharge Machining (EDM). Both sides of the specimens were ground to achieve a final thickness of approximately 2 mm and a gauge width of approximately 2.6 mm. To ensure reproducibility, three replicate experiments were conducted for each condition.

3. Results and discussion

3.1. Microstructure characterization of the base alloy

Fig. 1 presents the microstructure characterization of the as-cast BA. The EBSD image of the coarse macro-scale columnar grain is shown in Fig. 1(a). In an environment with a large solidification range and a high solidification rate, the α-Al dendritic structures form an unstable planar interface. At the same time, the α-Al dendritic structures, which are generally known to grow along the <100> direction, aligned with the direction of heat flow perpendicular to the mold wall. The α-Al dendritic structures in directions other than the <100> heat flow direction stop growing. As the temperature gradient decreases, secondary and tertiary dendrite arms form within the α-Al dendritic structures. The tertiary arms, which are similar in direction to the primary dendrite arm, consequently grow into one columnar grain composed of many primary dendrite arms [37]. It was confirmed that the average columnar size of the BA was ≥400 μm through equivalent circle diameter measurement after EBSD imaging. Fig. 1(b) and (c) show low-magnification and high-magnification SEM−SE images of the final solidified microstructure. In these images, coarse rounded phases with dendritic morphology, dual phases existing between the rounded phases, white needle-like and irregularly shaped phases, and black spherical phases are present. Fig. 1 (d) shows the composition distribution of each phase as confirmed via EDS analysis. The coarse rounded phases with dendritic morphology are identified as Al-rich α-Al dendritic structures, and the dual-phases regions existing between the rounded phases are eutectic phases composed of a Si phase (bright phase) and an Al phase (gray phase). The white phases at the interface of the α-Al dendritic structures and the eutectic Si were identified as Fe-rich intermetallic compounds (IMCs), while the dark-contrast phases were confirmed to be Mg-rich IMC. Although Fe was not intentionally added, it can be introduced in amounts of up to 5 wt% due to improper use of iron dissolution tools, prolonged holding of the molten metal, or the use of large amounts of Fe-containing scrap [38]. The solidification sequence of this microstructure can be predicted using a Scheil simulation with Thermo-Calc, as shown in Fig. 1(e). The yellow line represents the non-equilibrium solidification sequence calculated under the assumption of no diffusion in the solid phase and complete mixing in the liquid phase. Solidification begins at 585 °C, and at 555 °C, the remaining liquid undergoes a eutectic reaction to form eutectic phases. As cooling progresses, various stable types of IMCs precipitate, such as Mg_2Si, AlFeMnSi ($Al_9Fe_{0.84}Mn_{2.16}Si$), and grow. The schematic diagram in Fig. 1(e) illustrates the microstructural changes with temperature, based on the final solidified structure observed in Fig. 1(a)–(d) and the solidification sequence in Fig. 1(e). It was confirmed that the BA consists of relatively coarse α-Al dendritic structures, elliptical eutectic Si phases, and needle-like and irregularly shaped IMC phases during solidification.

3.2. Alloy design of high entropy microstructure refiner

Fig. 2 shows the alloying element selection criteria of HMR based on thermodynamic factors for grain refinement and the expected refinement mechanism that can collectively refine the α-Al dendritic structures and eutectic Si. The well-known refinement mechanism of hypoeutectic Al–Si alloy is the formation of heterogeneous nucleation

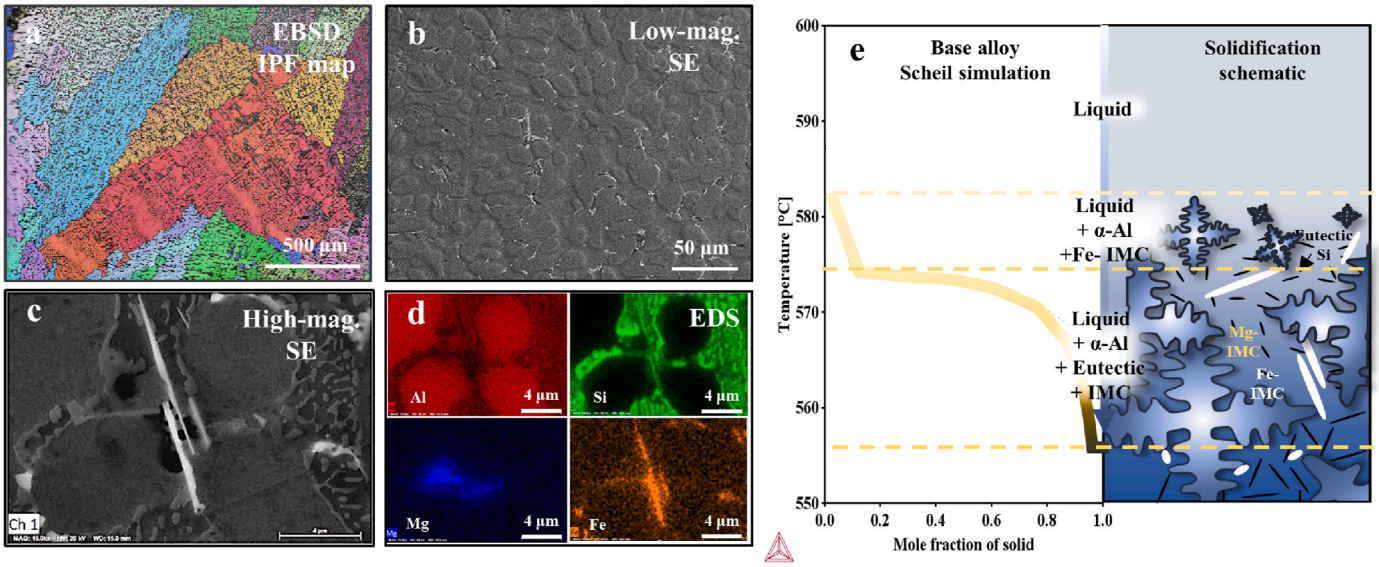

Fig. 1. Microstructure characterization of the as-cast base alloy
(a) EBSD Inverse Pole Figure map (IPF) image of coarse macroscale columnar grains in the BA, (b) Low-magnification SEM−SE image showing the final solidification microstructure, (c) High-magnification SEM−SE image showing α-Al dendritic structure, eutectic structures, and intermetallic compounds, (d) EDS elemental maps displaying the composition distribution of each phase, (e) Scheil simulation result predicting the solidification behavior, and a schematic diagram showing the microstructural changes with temperature.

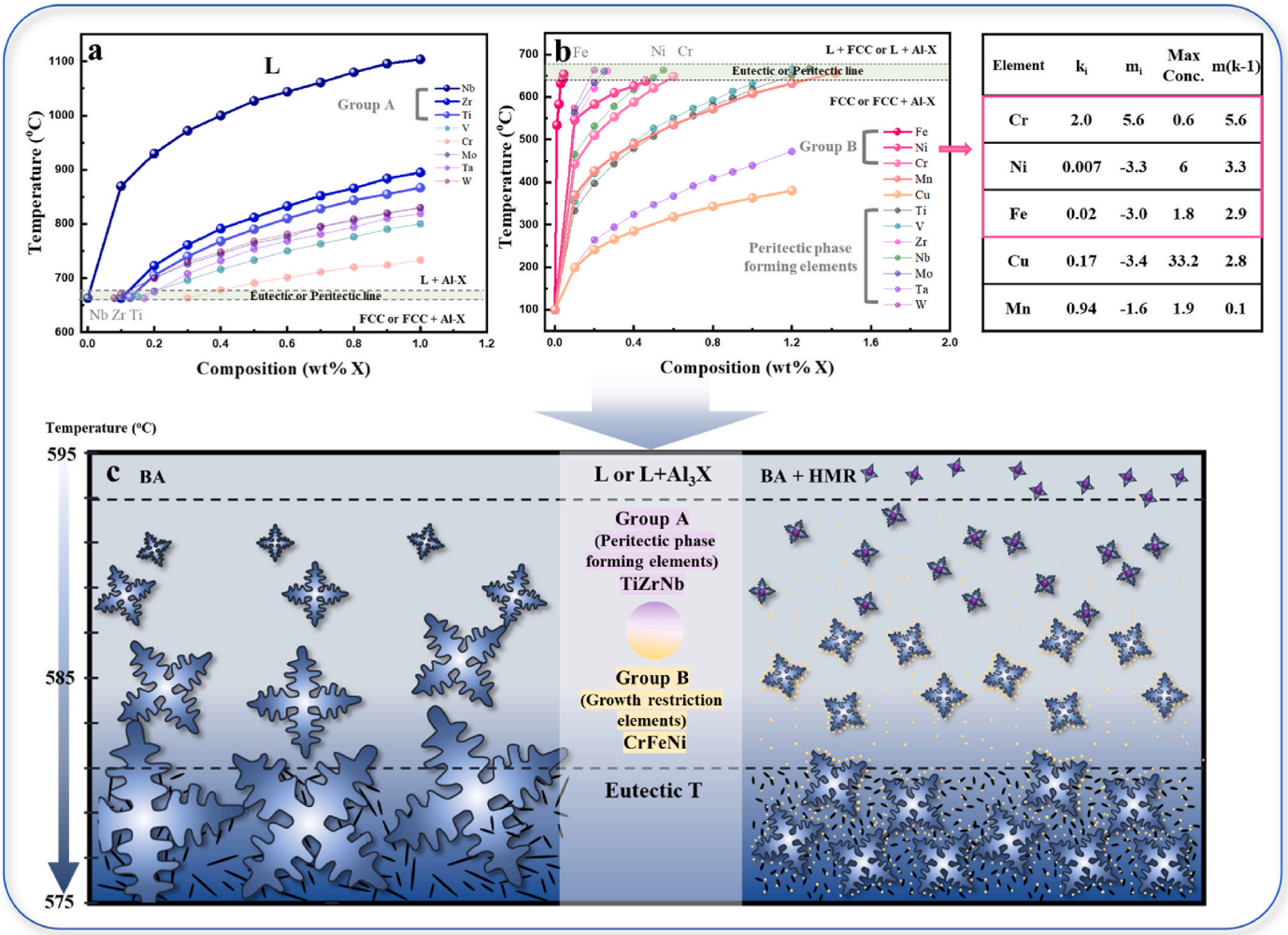

Fig. 2. Alloy design and refinement mechanism of high-entropy microstructure refiner (HMR)
Binary phase diagram in Al-enriched region of (a) Al-X (X = peritectic phase-forming elements = Nb, Zr, Ti, V, Cr, Mo, Ta, W) showing Al_3X phase formation temperatures and (b) Al-(Y or X) (Y = common alloying elements in Al alloy = Fe, Ni, Cr, Mn, Cu) showing solubility change. The inset table on the right side of Fig. 2 (b) summarizes *k* (partition coefficient), *m* (liquidus slope), max conc. (maximum concentration of L + S region) and m(k-1) (relative grain restriction factor) for Y elements. (c) Schematic representation of the expected refinement mechanism upon adding HMR composed of Group A and/or Group B elements to the base alloy.

sites and grain growth restriction via constitutional undercooling (ΔT_C) [39]. Firstly, the formation of heterogeneous nucleation sites is the refinement mechanism for α-Al dendritic structures. To refine the α-Al dendritic structures, a stable Al_3X phase should be formed at a temperature higher than the melting temperature of α-Al [30]. Fig. 2(a) shows the binary phase diagram in Al-enriched region of Al-X (X = peritectic phase-forming elements = Nb, Zr, Ti, V, Cr, Mo, Ta, W). Compared to other additive elements, Nb, Zr, and Ti exhibit higher Al_3X phase formation temperatures (Supplementary Table 1)—in that order. This makes them suitable candidates for stable Al_3X-forming elements. In particular, the elements Ti, Zr, and Nb exhibit edge-to-edge matching with Al, and Al_3Ti, Al_3Nb, and Al_3Zr all have a misfit within 10 %, allowing them to function effectively as heterogeneous nucleation sites [16,24,28,29]. Therefore, they act as stronger nucleation agents compared to conventional borides such as TiB_2, ZrB_2, NbB_2 [24]. Furthermore, the addition of Nb is known to significantly reduce the Si-poisoning effect, which is known to hinder α-Al dendritic structure refinement, due to the increased high-temperature phase stability of Al_3X [29]. J. Xu et al. reported that the coexistence of peritectic phase-forming elements promotes the precipitation of aluminide in Al–Si melts [40]. Secondly, grain growth restriction via inducing ΔT_C is known to limit the growth of α-Al dendritic structures due to the effect of high-density solute field present ahead of α-Al dendrite tip [41]. Fig. 2 (b) shows binary phase diagram in Al-enriched region of Al-(Y or X) (Y = common alloying elements in Al alloy = Fe, Ni, Cr, Mn, Cu) showing solubility change. Among the elements commonly added to Al–Si alloys, Fe (126 p.m.), Ni (124 p.m.), and Cr (128 p.m.), which have significantly smaller atomic sizes than Al (143 p.m.), exhibit low solubility with Al in that order, excluding the peritectic phase-forming elements. Additionally, the inset table on the right side of Fig. 2(b) summarizes *k* (partition coefficient), *m* (liquidus slope), and max conc. (maximum concentration of *L* + *S* region), determined from the Al–Y (Y=Fe, Ni, Cr, Mn, and Cu) binary phase diagrams shown in Supplementary Fig. 1 and calculated the relative magnitude of the grain restriction factor (*m* (k-1)). The grain restriction factor (Q) indicates the degree of grain refinement via ΔT_C of the additive elements and is expressed by the following equation [42].

$$Q = m_i C_0 (k - 1) \quad (1)$$

where k is the binary equilibrium partition coefficient, C_0 is the composition, and m_i is the liquidus gradient for each element *i*.

Among Cr (0.6 wt%), Fe (1.8 wt%), Ni (6 wt%), Cu (33.2 wt%), and Mn (1.9 wt%)—which have sufficient maximum concentrations—Cr (5.6), Ni (3.3), and Fe (2.9) have relatively high m(k-1) values, representing the relative magnitude of Q and their low solubility in Al. Therefore, a significant ΔT_C effect can be expected. Finally, we

categorized the peritectic phase-forming elements Ti, Zr, and Nb as Group A, and the growth-restriction elements Cr, Fe, and Ni as Group B, and added them to the BA in various ratios. Fig. 2(c) schematically illustrates the microstructural refinement mechanism induced by the addition of the HMR proposed in this study. At temperatures above the formation of the α-Al phase, Group A elements (Ti, Zr, Nb) react with aluminum in the melt to form Al_3X-type intermetallic compounds (X = Ti, Zr, Nb), which serve as heterogeneous nucleation sites for α-Al. This significantly reduces the nucleation undercooling, thereby facilitating the formation of numerous nuclei during the early stages of solidification and effectively refining the grain size of the α-Al phase. As solidification progresses and the α-Al phase grows, Group B elements (Cr, Fe, Ni) are rejected toward the L/S interface and become locally enriched in this region. This segregation induces ΔT_C, which suppresses the growth of secondary dendrite arms as well as eutectic Si, while simultaneously promoting new nucleation. Consequently, the developed HMR enables the simultaneous refinement of α-Al dendrites and eutectic Si through this combined mechanism. Furthermore, in this study, three elements from each of Group A and Group B were selected and combined in equiatomic ratios. These compositions correspond to typical BCC (Group A) and FCC (Group B) high-entropy alloy structures, which are known to exhibit excellent phase stability. While the individual elements within each group are known to provide grain refinement effects, they also possess large negative mixing enthalpies with Al and Si, which increases the tendency to form various intermetallic compounds during solidification when added individually. To overcome this issue, a high-entropy design strategy was employed by mixing the elements of each group in equiatomic proportions to promote the high-entropy effect and suppress the formation of undesirable intermetallic compounds during cooling.

The compositions of HMR in this study are shown in Table 1, and five different HMRs of 0.5 wt% were added to the BA, respectively. We compare the degree of grain refinement achieved by five different HMRs, which are mixed in the ratios of A, A_2B, AB, AB_2, and B (1:0, 2:1, 1:1, 1:2, 0:1) from the Group A and Group B. Fig. 3 indicates the pseudo-binary phase diagram between equiatomic TiZrNb and equiatomic CrFeNi. For HMR compositions consisting solely of Group A or Group B, each retains a BCC single phase for equiatomic TiZrNb (HMR-A) and an FCC single phase for equiatomic CrFeNi (HMR-B), respectively. For compositions where both Group A and Group B are added, numerous intermetallic compounds are predicted to primarily form. It is known that the two groups—Group A, which has relatively larger atomic sizes, and Group B, which has relatively smaller atomic sizes—form a stable Laves phase with a C14/C15 crystal structure [43]. Furthermore, the heat of mixing values between the elements of the two groups were confirmed to have large negative values (<-7 kJ/mol) using the Miedema model for binary alloys (Supplementary Fig. 2(a)). XRD phase analysis revealed that in the HMR compositions where Group A and Group B elements were simultaneously added, various combinations of C14/C15 Laves phases were formed (Supplementary Fig. 2(b)). As shown in Supplementary Fig. 3, Thermo-Calc simulations indicate that HMR compositions containing both Group A and Group B elements ($HMR\text{-}AB_2$, HMR-AB, and $HMR\text{-}A_2B$) form Laves phase-dominant or complex multi-phase microstructures coexisting with BCC phases. In addition, as presented in Supplementary Fig. 4(a), these compositions exhibit higher Vickers hardness compared to HMR-A and HMR-B, which are composed of single-phase BCC or FCC structures. Furthermore, the indentation traces indicate that crack formation is observed around the indentations in $HMR\text{-}AB_2$, AB, and A_2B, whereas plastic deformation of the matrix is primarily observed in HMR-A and HMR-B (Supplementary Fig. 4(b–f)). Laves phase intermetallic compounds exhibit strong brittleness and are characterized by fracturing without deformation under certain stress. As a result, the $HMR\text{-}A_2B$ to $HMR\text{-}AB_2$ compositions, which belong to the Laves phase-forming region marked by a green box in Fig. 3, can be pulverized through mechanical processes such as simple crushing and cutting methods without requiring specialized equipment. This provides an advantage in the easy addition and uniform dissolution of the refinement agent during the melting of BA. Furthermore, HMR-A, composed only of Group A, has a high melting point exceeding 2000K (1727 °C). By contrast, $HMR\text{-}A_2B$ to $HMR\text{-}AB_2$, composed of both Group A and Group B elements, have lower melting points compared to HMR-A. For example, $HMR\text{-}A_2B$ exhibits a relatively low melting point of about 1600K (1327 °C). Therefore, even though the HMR material with a Laves-phase microstructure may be used during the fabrication and addition to melt stages, the Laves phases—with their relatively low melting points—easily dissolve during melting and do not hinder grain growth. Specifically, as solidification progresses, Group A elements and Group B elements exhibit different behaviors at different stages, enabling stepwise control of the microstructure. Accordingly, the proposed refinement agent offers advantages in both manufacturing cost-efficiency and microstructural refinement effectiveness.

Table 1
Alloy compositions of (base alloy + high-entropy microstructure refiner) in this study.

Alloy	HMR Group (Designation)	HMR composition (at%)
BA (Silafont®-36) +0.5 wt% HMR-A	A	TiZrNb
BA (Silafont®-36) +0.5 wt% $HMR\text{-}A_2B$	A_2B	$(TiZrNb)_2(CrFeNi)$
BA (Silafont®-36) +0.5 wt% HMR-AB	AB	(TiZrNb)(CrFeNi)
BA (Silafont®-36) +0.5 wt% $HMR\text{-}AB_2$	AB_2	$(TiZrNb)(CrFeNi)_2$
BA (Silafont®-36) +0.5 wt% HMR-B	B	CrFeNi

3.3. Grain refinement effect of the high entropy microstructure refiner

Fig. 4 shows the high-energy XRD results and EBSD results showing the α-Al dendritic structure refinement performance for the BA and for (BA + HMR-A) to (BA + HMR-B) alloys. Generally, it is reported that in the XRD crystallization peaks of Al–Si–Mg alloys, α-Al and Si in the eutectic structure, Mg_2Si, AlFeMnSi, and Al_3X IMCs can be identified [44]. In this study, Al and Si major peaks, as well as Mg_2Si and AlFeMnSi minor peaks, were observed in Fig. 4(a) and Supplementary Fig. 5. Despite the addition of HMR, it was difficult to clearly identify the other IMC peaks in all compositions. Fig. 4(b) compares the size of the α-Al dendritic structures depending on the HMR compositions. The images shown within the graph were measured using SEM-EBSD mode, and the size of the α-Al dendritic structures was measured using the equivalent circle diameter measurement method. Under the same casting conditions, the α-Al dendritic structures of the unrefined BA were relatively coarse, with an average size of 410 ± 64.59 μm. In the HMR-added alloys, the refinement performance of the α-Al dendritic structures improved as the content of Group A increased. Specifically, in (BA + HMR-A) and (BA + $HMR\text{-}A_2B$) alloys, the average sizes were 75 ± 26.04 μm and 44.57 ± 13.88 μm, respectively. These reduction performances achieved were approximately 81.7 % for (BA + HMR-A) and 89.1 % for (BA + $HMR\text{-}A_2B$) compared to the BA. According to previous reports, the average grain size after refinement using conventional Al–Ti–B system refiners is 200–300 μm [16–18]. From the perspectives of the Hall-Petch effect and porosity control, an average grain size below 50 μm is highly desired in the industry [45]. The (BA + $HMR\text{-}A_2B$) alloy developed in this study achieves an average grain size below 44.57 ± 13.88 μm, demonstrating excellent α-Al dendritic structures refinement performance, and is suitable for commercial applications. Interestingly, among the (BA + $HMR\text{-}A_2B$), (BA + HMR-AB), and (BA + $HMR\text{-}AB_2$) alloys where both Group A and Group B were added, the α-Al dendritic structures refinement performance of the (BA + $HMR\text{-}A_2B$) alloy was notably superior. Therefore, to confirm the individual and complex microstructure refinement effects between Group A and Group B, further analysis was focused on (BA + HMR-A), (BA + HMR-B), and (BA +

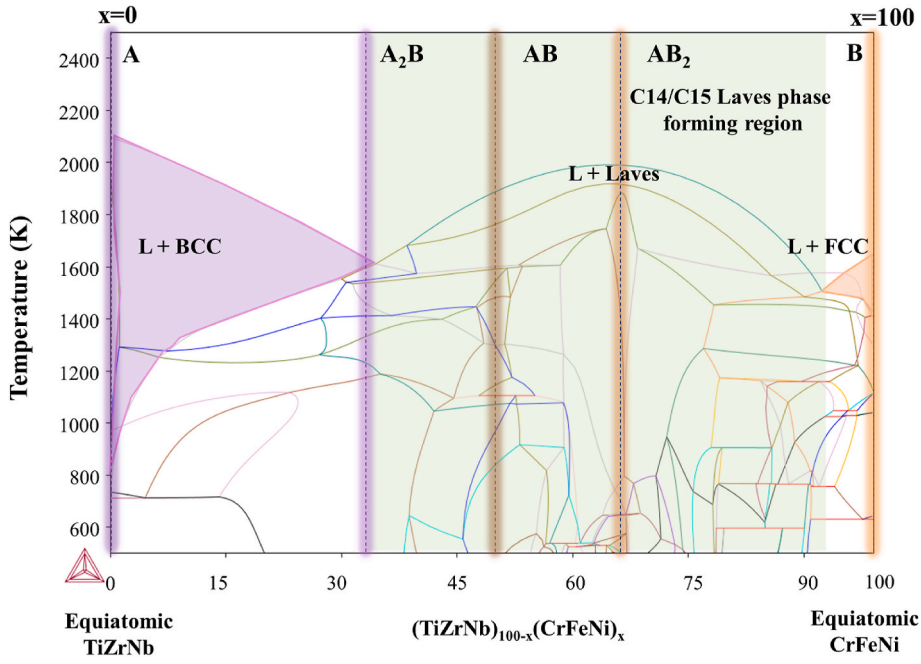

Fig. 3. Pseudo-binary phase diagram between equiatomic TiZrNb and equiatomic CrFeNi.
The compositions of the developed HMR are represented with dashed lines and neon highlights, and the ratios of each HMR are A, A_2B, AB, AB_2, and B. The green box indicates the Laves phase-forming region, which includes HMR-A_2B to HMR-AB_2 compositions.

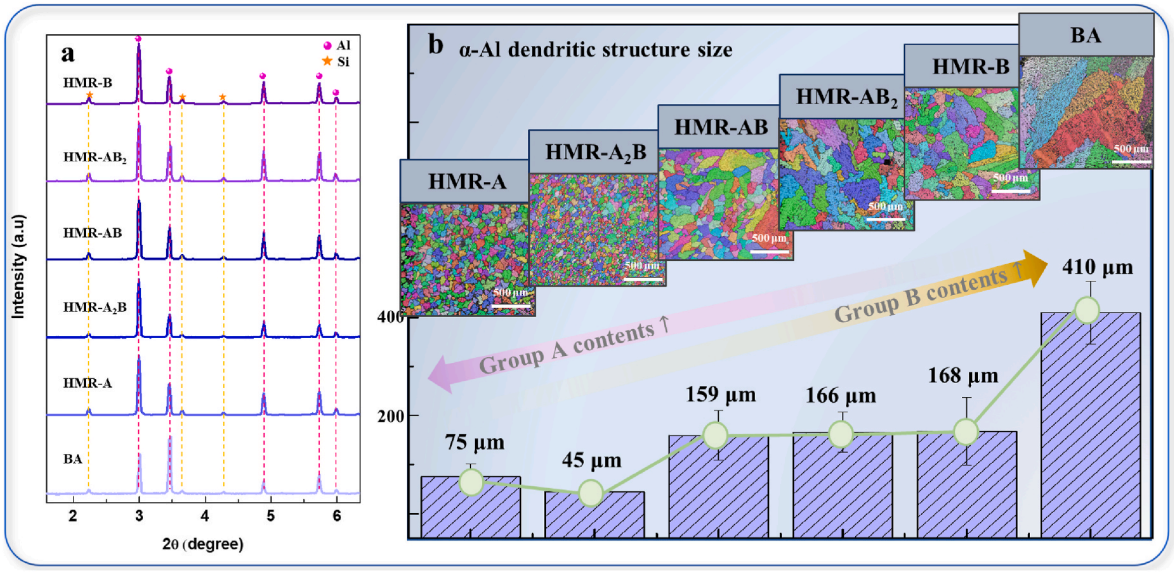

Fig. 4. α-Al dendrite refinement effect of high-entropy microstructure refiner
(a) High-energy XRD phase analysis of BA and (BA + HMRs) (b) EBSD IPF images and bar graph showing α-Al dendritic structure size difference depending on HMR compositions.

HMR-A_2B). Meanwhile, Easton and St. John [41] investigated the correlation between α-Al dendritic structure size (d), undercooling for active nucleation (ΔT_N), and the growth restriction factor (Q). The empirical equation is expressed as follows;

$$d = 1 \Big/ \sqrt[3]{\rho f} + D\Delta T_N \Big/ vQ \tag{2}$$

where ρ is the density of nucleant particles, f is the fraction of these particles that are activated, D is the diffusion coefficient; v is the growth velocity, ΔT_N is the undercooling for active nucleation, and Q is the growth restriction factor. According to Equation (2), it can be understood that the size of the α-Al dendritic structures is proportional to ΔT_N and inversely proportional to Q [36]. In the present study, all HMR refiners were introduced at the same contents and processed under identical cooling conditions; therefore, ΔT_N was adopted as the primary metric for comparing the relative nucleation potency of the developed refiners (HMRs). Here, ΔT_N can be determined by the difference between the liquidus temperature (T_L) and the crystallization temperature (T_x) of the material, both of which can be obtained through DSC analysis. Fig. 5 shows the DSC traces for (BA + HMR-A), (BA + HMR-A_2B), (BA + HMR-B), and BA at different heating rates. In the case of hypoeutectic Al–Si, the onset temperature of the melting peak is related to the

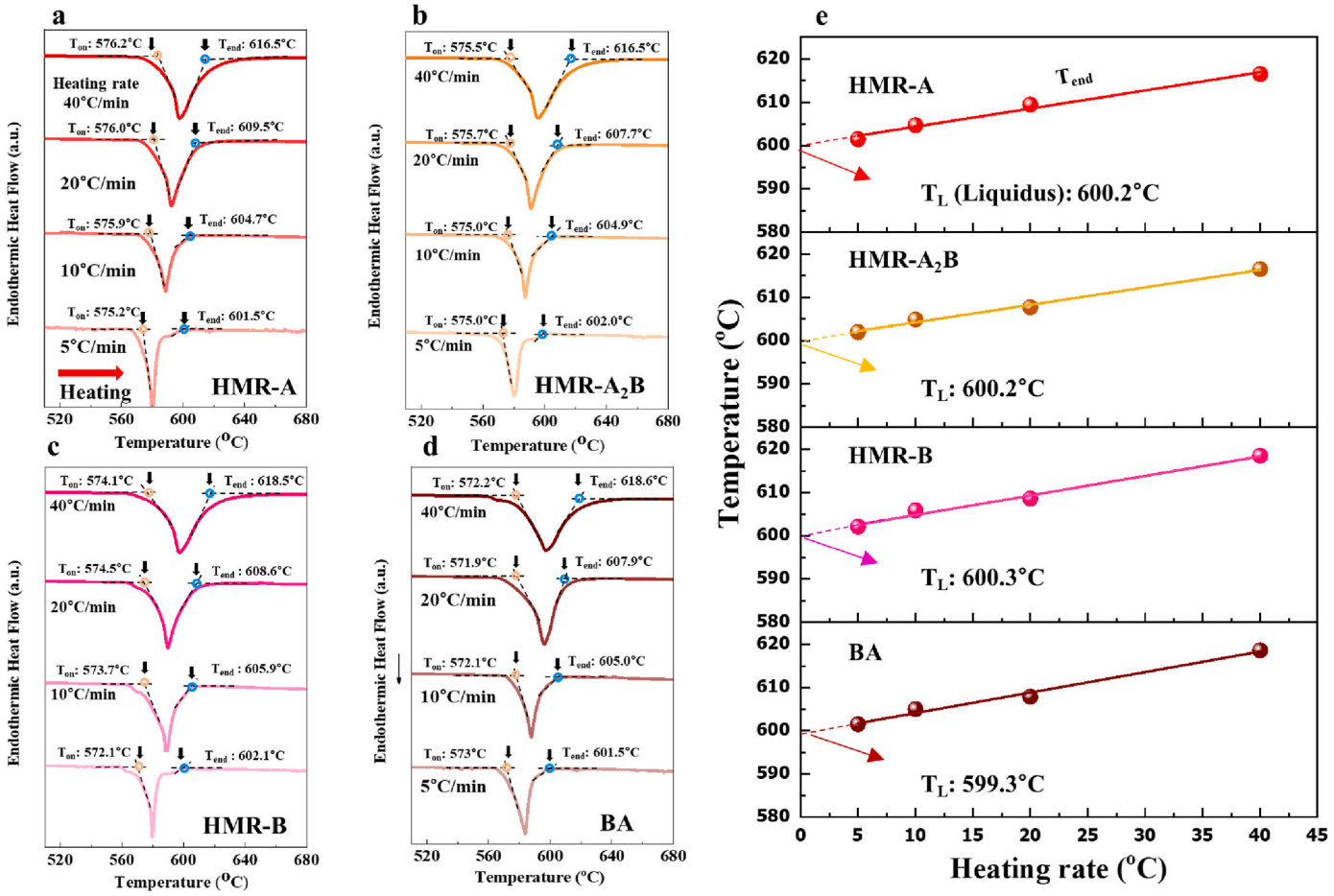

Fig. 5. DSC heating curves depending on high-entropy microstructure refiner compositions
DSC heating curves for (a) (BA + HMR-A), (b) (BA + HMR-A_2B), (c) (BA + HMR-B), and (d) BA (without HMR) at different heating rates of 5 °C/min, 10 °C/min, 20 °C/min, and 40 °C/min. The orange circle shows onset temperature of melting peak at different heating rates. The blue circle shows endset temperature of melting peak at various heating rates. (e) Variation of endset temperature of melting peak depending on heating rates, fitted by straight line. Extrapolation to 0 °C/min represent T_L of the alloy.

melting of the eutectic reaction. Subsequently, the broad endothermic effect signifies the melting of the remaining solid components. Therefore, the endset temperature of the melting peak is associated with the T_L [46]. Fig. 5(a) shows the heating curves of the (BA + HMR-A) at heating rates ranging from 5 °C/min to 40 °C/min. The onset temperature, where melting begins during heating, has similar values (575.2–576.2 °C) across different heating rates. In contrast, the endset temperatures for heating rates of 5 °C/min, 10 °C/min, 20 °C/min, and 40 °C/min are 601.5 °C, 604.7 °C, 609.5 °C, and 616.5 °C, respectively, showing variations of the values depending on the heating rate. Therefore, to obtain the T_L, it is necessary to exclude the influence of the heating rate when obtaining the endset temperature. To determine the T_L, a very slow heating rate is required, which involves substantial time and economic costs. Meanwhile, E. B. Ferreira et al. [47] proposed a method to determine the T_L by obtaining the endset temperatures of the melting peaks at various heating rates for glasses and using extrapolation. In this study, we applied this method to determine the T_L of the (BA + HMR) alloys. Using these data, we plotted the endset temperature of the melting peak versus the heating rate and fitted straight lines to the data. By extrapolation, we determined the T_L of the (BA + HMR-A) at a heating rate of 0 °C/min, as shown at the top of Fig. 5(e). Using the same method, the DSC results for measuring the onset and endset temperatures of (BA + HMR-A_2B), (BA + HMR-B), and BA are shown in Fig. 5 (b)–(d). The T_L at 0 °C/min obtained by extrapolation is presented in Fig. 5(e). The T_L values of (BA + HMR-A), (BA + HMR-A_2B), (BA + HMR-B), and BA were 600.2 °C, 600.2 °C, 600.3 °C, and 599.3 °C, respectively. Fig. 6 shows the DSC traces for (BA + HMR-A), (BA + HMR-A_2B), (BA + HMR-B), and BA at different cooling rates. Fig. 6(a) shows the cooling curve of (BA + HMR-A) at cooling rates of 5 °C/min, 10 °C/min, 20 °C/min, and 40 °C/min. The onset temperature of the crystallization peak during cooling is associated with the crystallization of the α-Al dendritic structures. The onset temperatures at cooling rates of 5 °C/min, 10 °C/min, 20 °C/min, and 40 °C/min were 597.4 °C, 596.2 °C, 595.3 °C, and 594.5 °C, respectively. The results for ΔT_N, which is the difference between the T_L and the T_X for the α-Al dendritic structures, are shown in top of Fig. 6(e). Using the same method, the results of the α-Al dendrite crystallization peaks for (BA + HMR-A_2B), (BA + HMR-B), and BA are shown in Fig. 6(b)–(d). The calculated ΔT_N (=T_L-T_X) values, depending on the HMR compositions and cooling rates, are presented in Fig. 6(e). The detailed data of the corresponding DSC thermal information and the T_L and ΔT_N values are presented in Table 2. The (BA + HMR-A) and (BA + HMR-A_2B) alloys, which exhibit excellent α-Al dendritic structure refinement performance with grain sizes below 100 μm, have ΔT_N values of 5.1 °C and 6.4 °C, respectively, at a cooling rate of 40 °C/min. This represents a significant reduction by one-quarter compared to the ΔT_N of BA. This indirectly proves that larger heterogeneous nucleation sites were formed in the (BA + HMR-A) and (BA + HMR-A_2B) alloys, resulting in fine α-Al dendritic structure sizes, as shown in the EBSD images in Figs. 4(b) and 6(e). It should be noted that despite having a relatively larger ΔT_N value compared to (BA + HMR-A), (BA + HMR-A_2B) exhibits finer α-Al dendritic structure sizes. Furthermore, (BA + HMR-B) shows approximately 0.7 °C decreases of ΔT_N

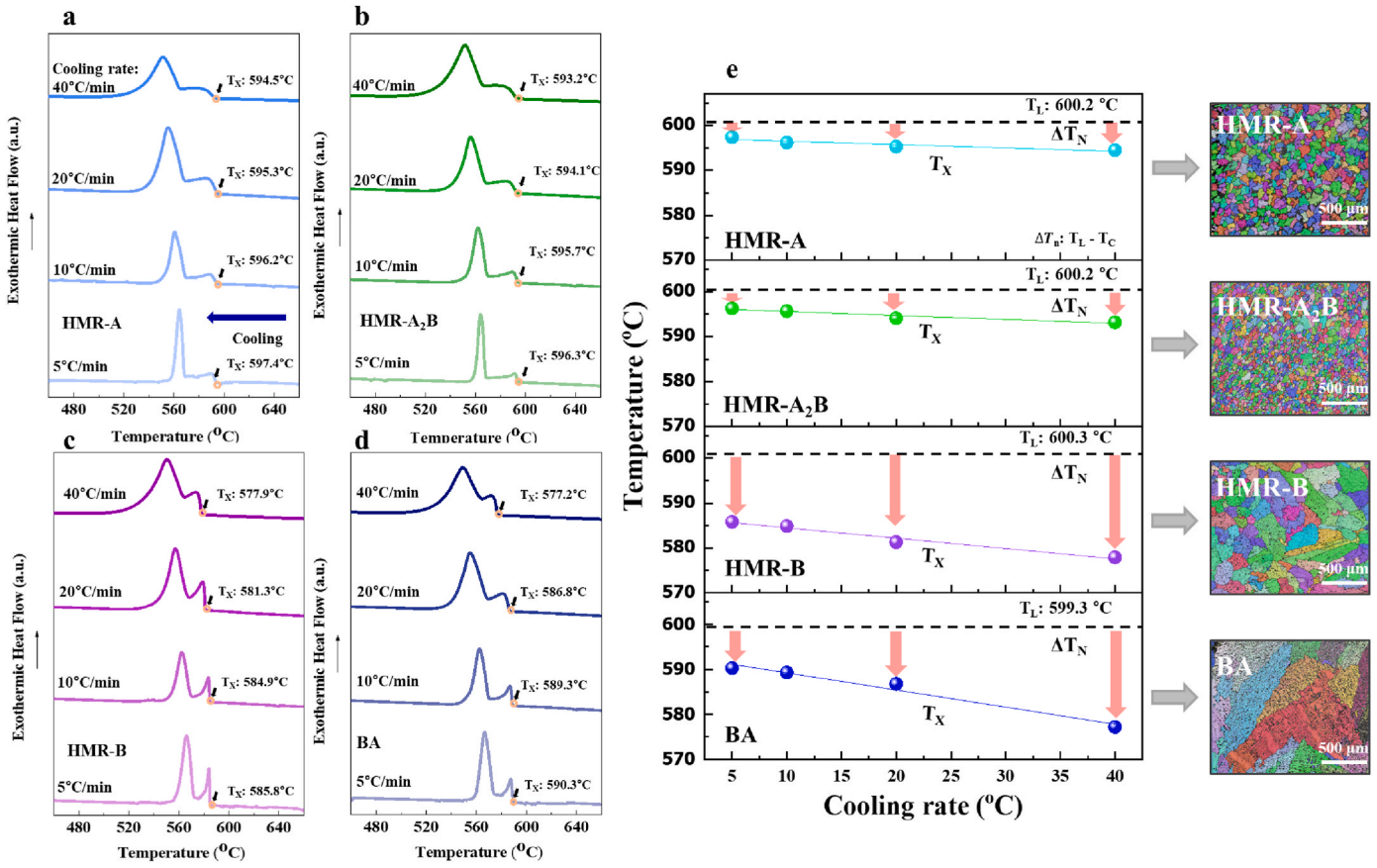

Fig. 6. DSC cooling curves depending on high-entropy microstructure refiner compositions
DSC cooling curves for (a) (BA + HMR-A), (b) (BA + HMR-A2B), (c) (BA + HMR-B), and (d) BA (without HMR) at different cooling rates of 5 °C/min, 10 °C/min, 20 °C/min, and 40 °C/min. The orange circle shows onset temperature of crystallization peak at various cooling rates. (e) Variation of ΔT_N values (= difference between the liquidus temperature and the onset temperature of the α-Al crystallization peak) depending on cooling rates for (BA + HMR-A), (BA + HMR-A2B), (BA + HMR-B), and BA.

Table 2
The characteristic transformation temperatures (T_{end}, T_x, T_L) and Δ T_N of (BA + HMR-A), (BA + HMR-A_2B), (BA + HMR-B), and BA (without HMR).

Alloy	HMR Group	Characteristic transformation temperature									
		T_{end} (°C)				T_X (°C)				T_L(°C)	Δ T_N (°C) (=T_L-T_X)
		Heating rate (°C/min)				Cooling rate (°C/min)					
		5	10	20	40	5	10	20	40		
BA + HMR-A	**A**	601.5	604.7	609.5	616.5	597.4	596.2	595.3	594.5	600.2	5.1
BA + HMR-A_2B	**A_2B**	602.0	604.9	607.7	616.5	596.3	595.7	594.1	593.2	600.2	6.4
BA + HMR-B	**B**	602.1	605.9	608.6	618.5	585.8	584.9	581.3	577.9	600.3	21.7
BA	**-**	601.5	605.0	607.9	618.6	590.3	589.3	586.8	577.2	599.3	22.4

compared to the ΔT_N of BA at a cooling rate of 40 °C/min, but still achieves around 45 % α-Al dendritic structure refinement performance. Both the HMR-A_2B and HMR-B compositions contain Group B, and the elements in Group B are known to contribute to the growth restriction of α-Al dendritic structures. According to Equation (2), the size of the α-Al dendritic structures is correlated with ΔT_N and the growth restriction factor Q, so the influence of Group B elements in the HMR can also be expected. The Q value of this alloy was calculated using the equation below, excluding peritectic phase-forming elements with an extremely low maximum solute concentration [48].

$$Q_{Total} = \sum m_{Li} C_{0i} (k_i - 1) \quad (3)$$

where m_L is the slope of the liquidus, C_0 is the initial solute concentration, k is the equilibrium partition coefficient, and i refers to the individual solute in the multicomponent system.

The Q_{Total} of the BA and (BA + HMR-A), which do not contain Group B, is 1.17, while the Q_{Total} of (BA + HMR-A_2B) and (BA + HMR-B) is 1.71 and 2.78, respectively, which are 0.54 and 1.61 higher than that of the BA or (BA + HMR-A). Considering these two factors, it is concluded that the combined addition of the two groups leads to (BA + HMR-A_2B) having a synergistic effect of a low ΔT_N value and a high Q value, resulting in an excellent refinement effect on the α-Al dendritic structures. Moreover, even though Group A was not included, it is concluded that (BA + HMR-B), which has a high Q value, also leads to the refinement of the α-Al dendritic structures compared to the BA. Fig. 7 shows the secondary dendrite arm spacing (SDAS) refinement performance according to the HMR composition. As shown in Fig. 7(a), SDAS was measured using the following equation [49].

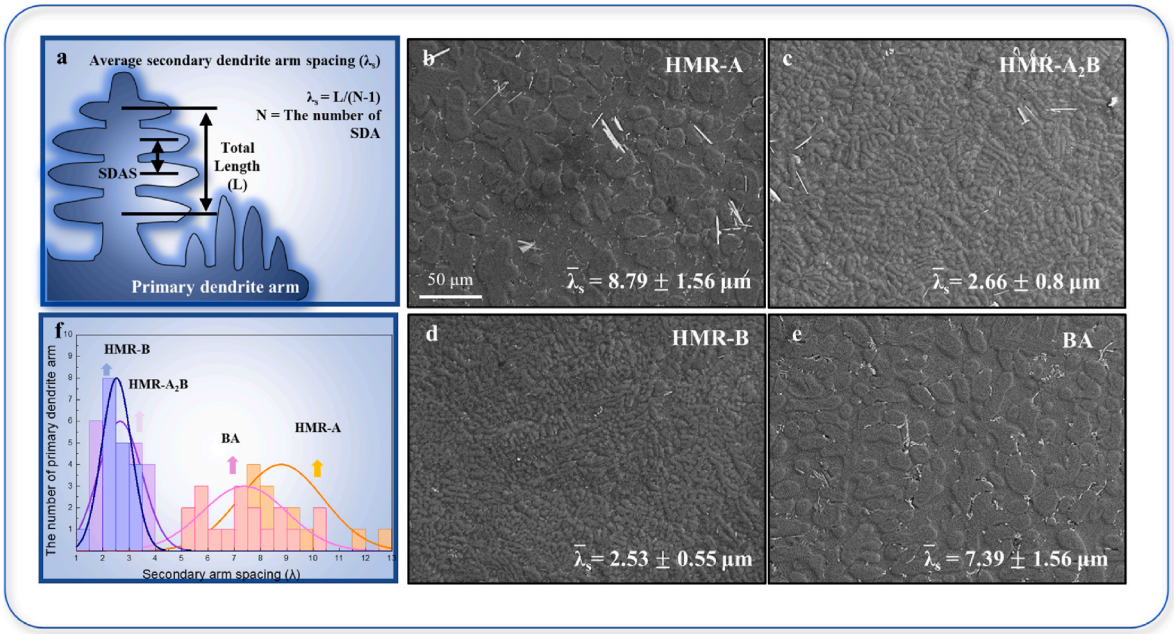

Fig. 7. Secondary dendrite arm spacing refinement effect of high-entropy microstructure refiner
(a) Schematic representation for measuring secondary dendrite arm spacing (SDAS) using the formula SDAS = L/(N-1), SEM SE images of (b) (BA + HMR-A), (c) (BA + HMR-A_2B), (d) (BA + HMR-B), and (e) BA (without HMR) showing the dendritic structure and measured average SDAS, (f) Distribution histogram of SDAS values from approximately 20 primary dendrite arms for each composition.

$$SDAS = L / (N - 1) \quad (4)$$

Here, the total length of the primary dendritic arm was measured as L, and the number of secondary arms, N, was counted exclusively along one side. Fig. 7(b)–(e) represent the SEM images of the central region of the specimens for (BA + HMR-A), (BA + HMR-A_2B), (BA + HMR-B), and BA, respectively. The average SDAS values are 8.79 ± 1.56 μm, 2.66 ± 0.8 μm, 2.53 ± 0.55 μm, and 7.39 ± 1.56 μm, respectively. Fig. 7(f) shows the distribution histogram of SDAS obtained from approximately 20 primary dendrite arms for each alloy. (BA + HMR-A_2B) and (BA + HMR-B), which contain Group B, show around 64 % and 65 % SDAS refinement performance compared to the SDAS of BA. In contrast, (BA + HMR-A), composed solely of Group A, did not exhibit SDAS refinement. This grain refinement of SDAS according to HMR compositions also has the same trend in the edge region, where the cooling rate is expected to be faster due to its proximity to the mold wall (Supplementary Fig. 6 (a–d)). Fig. 8 presents the SEM−SE images and the measurement results of the eutectic Si interlamellar spacing according to the HMR

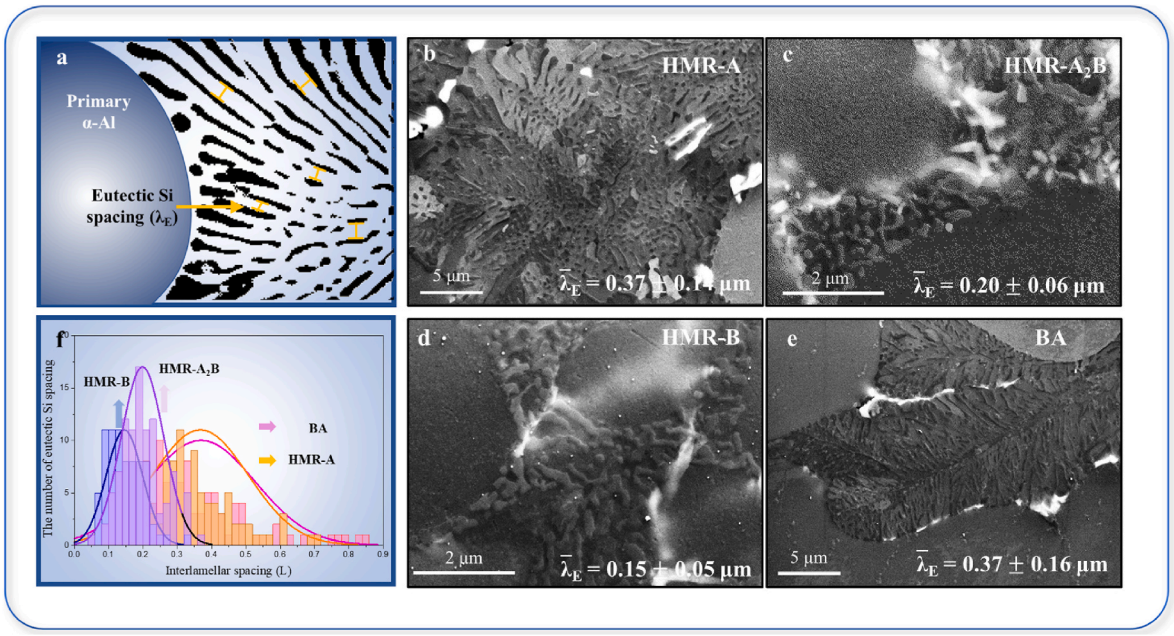

Fig. 8. Eutectic Si spacing refinement effect of high-entropy microstructure refiner
(a) Schematic diagram illustrating the method for measuring eutectic Si spacing, high magnification SEM image of (b) (BA + HMR-A), (c) (BA + HMR-A_2B), (d) (BA + HMR-B), and (e) BA (without HMR) showing the eutectic Si morphology and measured average eutectic Si spacing, (f) Distribution histogram of eutectic Si spacing values from approximately 100 measurement points for each composition.

compositions. Fig. 8(a) shows the method for measuring eutectic Si spacing as a schematic diagram. Fig. 8(b)–(e) correspond to the SEM images of (BA + HMR-A), (BA + HMR-A_2B), (BA + HMR-B), and BA, respectively. The average eutectic Si spacing for (BA + HMR-A), (BA + HMR-A_2B), (BA + HMR-B), and BA are 0.37 ± 0.14 μm, 0.20 ± 0.06 μm, 0.15 ± 0.05 μm, and 0.37 ± 0.16 μm, respectively. Fig. 8(f) shows the distribution histogram of eutectic Si spacing obtained from approximately 100 points for each composition. (BA + HMR-A_2B) and (BA + HMR-B), which contain Group B, exhibit approximately 45.9 % and 59.5 % eutectic Si refinement performance compared to the BA. In contrast, (BA + HMR-A), composed solely of Group A, did not exhibit eutectic Si spacing refinement. This grain refinement of eutectic Si spacing according to HMR compositions also has the same trend in the edge part (Supplementary Fig. 6(e–h)). Interestingly, as shown in Figs. 7 and 8, and Supplementary Fig. 7, the α-Al dendrite structure size of (BA + HMR-B) is coarser than that of (BA + HMR-A) and (BA + HMR-A_2B), whereas the SDAS and eutectic Si spacing are finer compared to those of the other two alloys. According to the general concept of grain growth

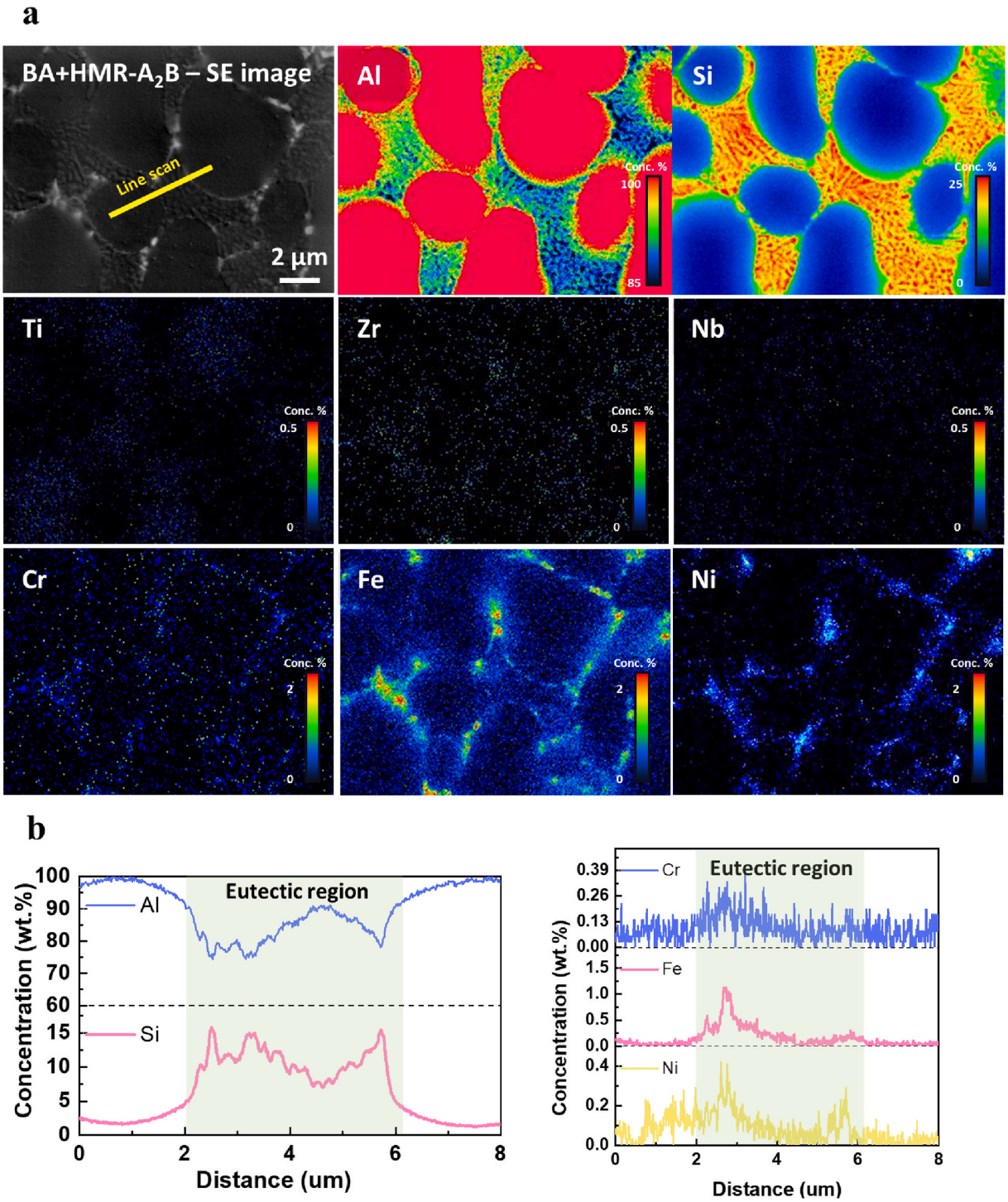

Fig. 9. EPMA mapping and line analysis of BA + HMR-A_2B
(a) EPMA mapping results for the elements Al, Si, Ti, Zr, Nb, Cr, Fe, and Ni. (b) Line scan analysis was performed along the yellow line indicated in the SE image of Fig. 9(a), The eutectic region (green box) shows the concentration gradients of Al, Si, Cr, Fe, and Ni.

restriction with increasing cooling rate, α-Al dendrite structure size, SDAS, and eutectic Si spacing should all decrease uniformly. However, since the cooling rates of the specimens in this study are nearly identical, this phenomenon can be clearly interpreted as the effect of HMR composition. As explained through Fig. 2(b) and Equation (3), Group B elements have a large maximum concentration and grain restriction factor (Q), which increases ΔT_C due to the segregation of Group B elements at the L/S interface. To investigate the segregation behavior of Group B elements, Fig. 9 presents the results of EPMA analysis performed on the BA + HMR-A_2B specimen, which exhibited refinement in both SDAS and eutectic Si, to investigate the evidence of segregation behavior of Group B elements. Fig. 9(a) shows the EPMA mapping results for Al, Si, Ti, Zr, Nb, Cr, Fe, and Ni. The α-Al dendritic structure is composed almost entirely of Al, while Si is mainly distributed in the eutectic region. Group A elements which form peritectic phases, tend to form Al_3X (X = Ti, Zr, Nb) phases early during solidification from the liquid, and thus are scarcely distributed in either the α-Al dendrite or the eutectic region. In contrast, Group B elements are concentrated in the eutectic region. Fig. 9(b) shows the results of a line scan conducted along the yellow line indicated in the SE image of Fig. 9(a). Cr, Fe, and Ni were found to segregate at the interface between the α-Al dendrite and the eutectic region, with a clear concentration gradient extending into the eutectic region. To validate the segregation behavior of Group B elements, additional EPMA analysis was conducted on the BA + HMR-B specimen, as shown in Supplementary Fig. 8. Similar to the trend observed in BA + HMR-A_2B, Cr, Fe, and Ni were found to be enriched at the interface between the α-Al dendrites and the eutectic Si phase. Based on these theoretical and experimental results, it is inferred that the Cr, Fe, and Ni atoms accumulated ahead of the α-Al dendrite front generate a strong concentration gradient at the L/S interface, thereby inducing localized ΔT_C. An increase in ΔT_C destabilizes the primary dendrite interface and promotes perturbations in the formation of secondary dendrites [50]. Additionally, solutes concentrated at the L/S interface contribute to the solute drag effect, where part of the driving force required for interface migration is consumed by friction between the solute atoms and the moving interface. The already formed solute enriched layer at the interface also hinders solute-solvent diffusion, further reducing the effective driving force for interface movements. As a result, this mechanism is effective in refinement SDAS. As a result, instead of a few secondary dendrite arms or eutectic Si phases growing significantly, multiple secondary dendrite arms are more likely to develop, leading to finer spacing between them [37,51]. Through the mechanisms of TPRE and IIT, eutectic Si typically grows in plate-like or needle-like morphologies. However, due to the influence of Group B elements present at the interface between eutectic Si and eutectic Al, solute atoms can adsorb onto twin planes or accumulate ahead of the

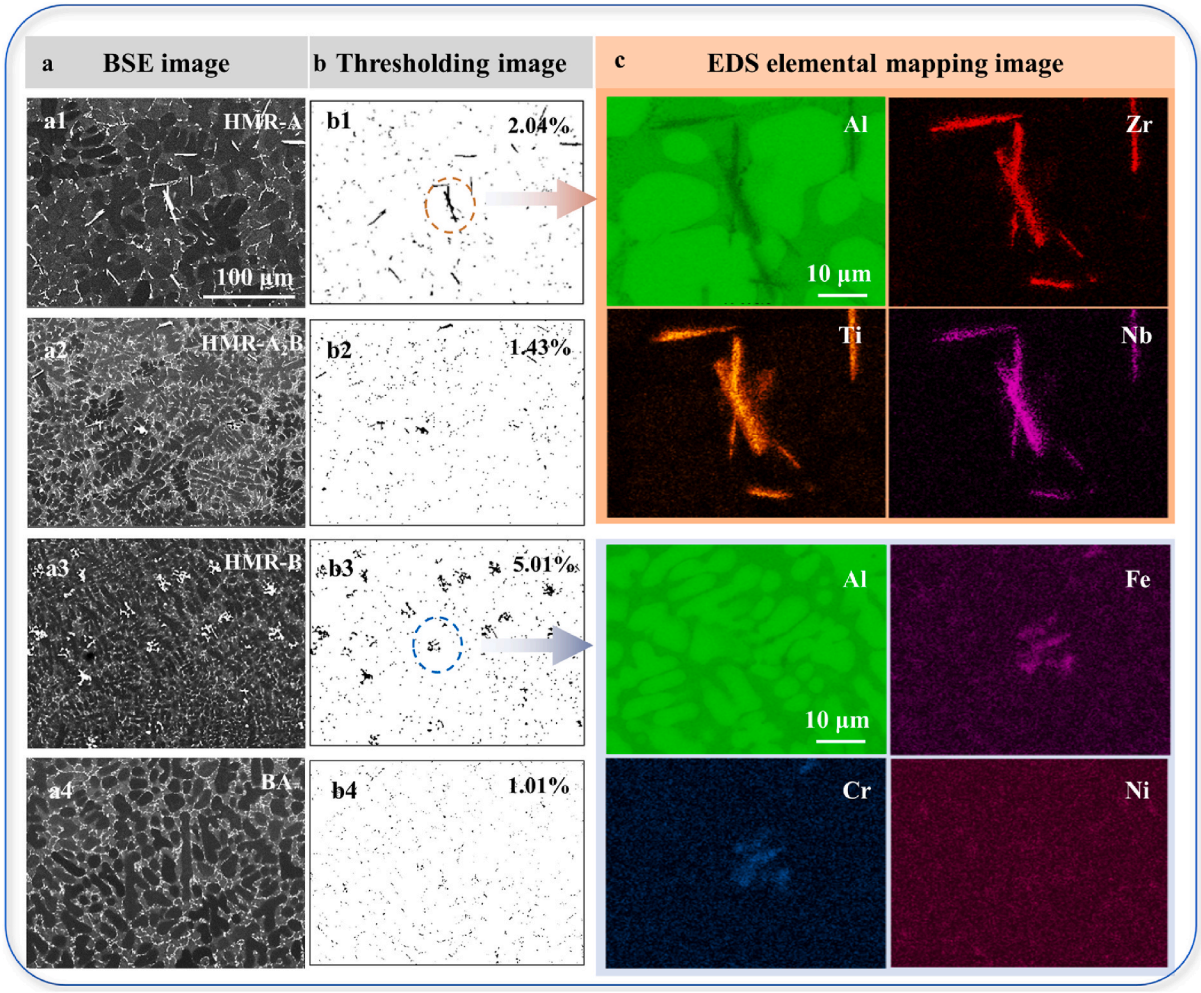

Fig. 10. Comparison of intermetallic compound fraction depending on HMR compositions
SEM-BSE mode images of the (a1) (BA + HMR-A), (a2) (BA + HMR-A_2B), (a3) (BA + HMR-B), and (a4) BA (without HMR), showing the distribution of intermetallic compounds as bright area, (b1–4) Thresholding images reconstructed from the SEM-BSE images using the ImageJ program. The dark areas correspond to the coarse intermetallic compounds, and the measured fractions of these compounds are indicated, (c) EDS elemental mapping images of intermetallic compounds in (b1) and (b3). EDS elemental mapping images exhibit needle-like intermetallic compounds in (b1) image and Chinese script like intermetallic compounds in (b3) image.

interface. This results in significant suppression of interface migration due to friction between the solute and the moving front, as well as restricted solute-solvent diffusion, ultimately leading to the formation of fine fibrous Si. [52–54]. Based on the above experimental results and theoretical evidence, it was confirmed that (BA + HMR-A_2B) and (BA + HMR-B), which contain Group B, exhibit superior SDAS and eutectic Si spacing refinement performance compared to (BA + HMR-A) and BA without HMR, which does not contain Group B. In particular, HMR-A_2B demonstrates the simultaneous refinement of α-Al dendritic structure size, SDAS, and eutectic Si spacing. On the other hand, the Group A and Group B elements utilized in this study may form intermetallic compounds that cause stress concentration during deformation when added above a certain content level, potentially leading to a deterioration of mechanical properties. Therefore, Fig. 10 indicates the results comparing the fraction of intermetallic compounds according to the HMR composition. Fig. 10(a) shows the SEM-BSE mode images of (BA + HMR-A), (BA + HMR-A_2B), (BA + HMR-B), and BA, while Fig. 10(b) is the thresholding image reconstructed from Fig. 9(a) images using the ImageJ program. The relatively bright areas in the BSE mode images and the dark areas in the thresholding images represent the coarse intermetallic compounds, and their measured fractions are noted. Compared to BA, the fractions of intermetallic compounds in (BA + HMR-A), (BA + HMR-A_2B), and (BA + HMR-B) increased by +1.04 %, +0.43 %, and +4.00 %, respectively. As shown in the EDS results in Fig. 10(c), (BA + HMR-A) forms needle-like TiZrNb intermetallic compounds, while (BA + HMR-B) predominantly forms a network of CrFeNi compounds. In contrast, in (BA + HMR-A_2B), where both Group A and Group B are added simultaneously, the fraction and size of intermetallic compounds significantly decrease. This indicates that the type and fraction of intermetallic compounds vary significantly depending on the compositional ratio of the HMR. In particular, HMR-A_2B minimizes the formation of additional compounds within the matrix while simultaneously refining both the α-Al dendritic structures and eutectic Si phases, demonstrating that it is a high-performance refiner capable of synergistic multi-phase microstructure refinement.

3.4. Grain refinement performance of high entropy microstructure refiner

Fig. 11 shows the results comparing the grain refinement performance of HMR and reported refiners. Fig. 11(a) shows a comprehensive evaluation of the microstructure of the BA and the (BA + HMR) alloys. In the case of (BA + HMR-A), which is composed of only Group A elements, it demonstrates superior α-Al dendritic structure grain refinement compared to the BA. In the case of (BA + HMR-B), which is composed solely of Group B elements, it shows a superior refinement effect on the secondary dendrite arm spacing and eutectic Si spacing compared to the BA. Notably, (BA + HMR-A_2B), which is composed of both Group A and Group B elements, demonstrates excellent refinement effects on the α-Al dendritic structures, SDAS, and eutectic Si spacing compared to the BA, while also exhibiting a significantly lower fraction of intermetallic compounds compared to (BA + HMR-A) and (BA + HMR-B). Interestingly, HMR-A_2B exhibits a more pronounced refinement effect on the α-Al dendritic structure compared to HMR-A, despite containing a lower amount of Group A elements. This is likely because the BA + HMR-A_2B composition does not lead to the formation of additional intermetallic compounds (Fig. 10(a2) and (b2), while containing an optimized

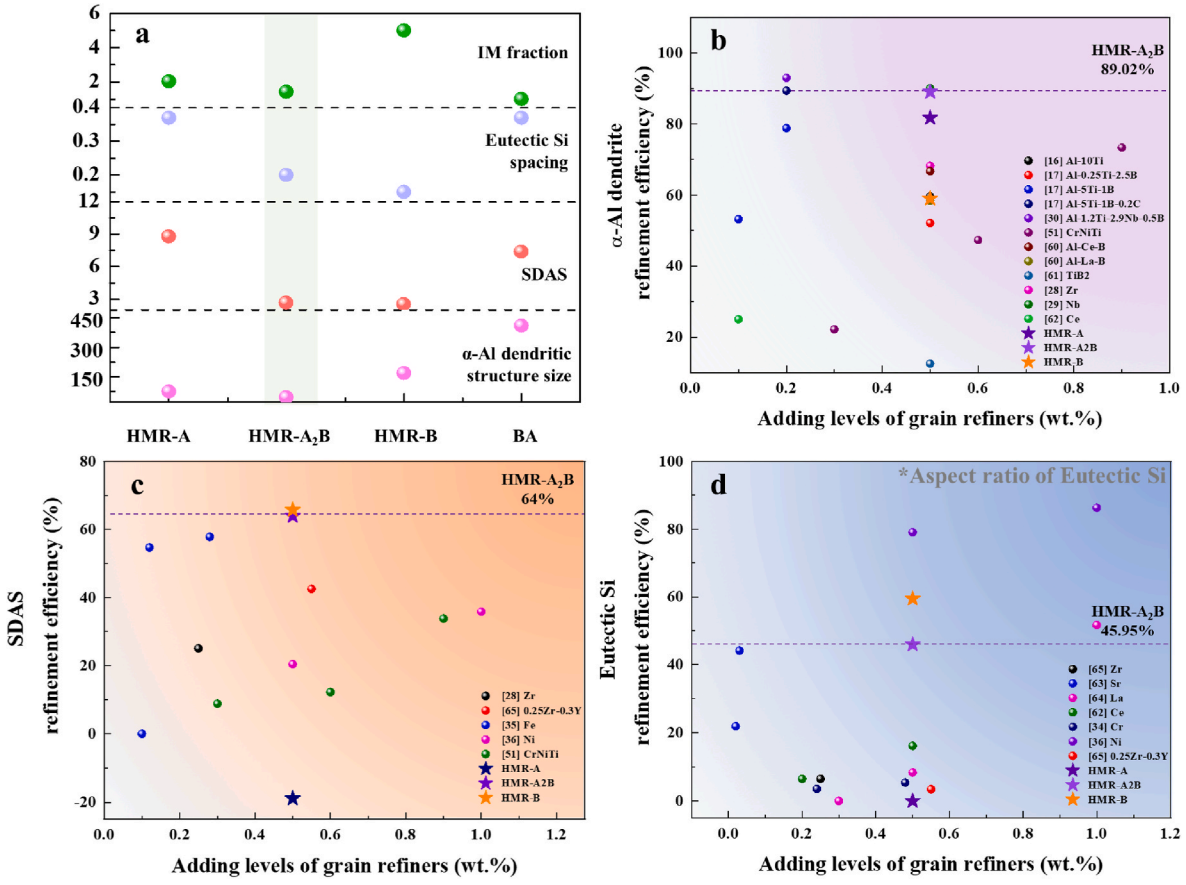

Fig. 11. Comparison of grain refinement performance among HMRs and previously reported refiners
(a) Summary of the microstructural evaluation in the (BA + HMR-A), (BA + HMR-A_2B), (BA + HMR-B), and BA, Comparison of (b) α-Al dendrite refinement efficiency [16,17,28–30,51,60–62], (c) secondary dendrite arm spacing refinement efficiency [28,35,36,51,65] and (d) eutectic Si refinement efficiency among developed HMRs in this study and previously reported refiners [34,36,62–65]. The star mark indicated HMR-A, HMR-A_2B and HMR-B in this study.

amount of Group A elements that maximizes the formation of heterogeneous nucleation sites. Furthermore, during solidification, certain Group B elements are locally segregated at the L/S interface (Fig. 9), and the resulting drag effect is believed to impede grain growth and movement. This phenomenon may contribute not only to the refinement of SDAS and eutectic Si but also enhances the refinement of the α-Al dendritic structure. Fig. 11(b)–(d) respectively compare (b) the α-Al dendritic structure refinement efficiency, (c) SDAS refinement efficiency, and (d) the eutectic Si refinement efficiency of the reported refiners and the HMRs in this study. The star marks indicate HMR-A, HMR-A_2B, and HMR-B in this study. The values indicated by the dashed lines represent the refinement efficiency of HMR-A_2B. Notably, HMR-A_2B exhibits α-Al dendritic structures refinement efficiency, SDAS refinement efficiency, and eutectic Si refinement efficiency of 89.02 %, 64 %, and 59.02 %, respectively. These results demonstrate HMR addition in Al alloys cause to excellent simultaneous refinement efficiency of complex microstructures compared to those of reported refiners.

3.5. Mechanical properties

Fig. 12 shows the uniaxial tensile properties of (BA + HMR-A), (BA + HMR-A_2B), (BA + HMR-B), and BA, along with a comparison of the tensile properties of previously reported refined alloys. Fig. 12(a) and **(b)** presents the engineering stress-strain curve and uniaxial tensile properties of (BA + HMR-A), (BA + HMR-A_2B), (BA + HMR-B), and BA. (BA + HMR-A) exhibited a similar yield strength, while (BA + HMR-A_2B) and (BA + HMR-B) showed increases of approximately 9.1 % and 5.9 %, respectively, compared to BA. Notably, (BA + HMR-A_2B) demonstrated the finest α-Al dendritic structures and secondary dendrite arm spacing (SDAS) among the alloys.

The ultimate tensile strength of (BA + HMR-A) and (BA + HMR-A_2B) increased by approximately 2 % and 9.6 %, respectively, compared to that of BA, while (BA + HMR-B) showed a value nearly similar to that of BA. In terms of elongation, (BA + HMR-A) and (BA + HMR-A_2B) exhibited increases in ductility of approximately 0.1 % and 14.8 %, respectively, compared to that of BA, whereas (BA + HMR-B) showed a reduction in ductility of about 35 %. The refinement of both α-Al dendrites and eutectic Si leads to an increased interfacial area between the α-Al dendrite and the eutectic regions, which acts as an effective barrier to dislocation motion. As a result, strength enhancement occurs via the well-known Hall–Petch mechanism [55]. In addition, finer dendritic structures reduce the size and connectivity of shrinkage pores and micro-voids, thereby decreasing the likelihood of void coalescence during deformation and ultimately improving ductility [56,57]. Furthermore, reducing the size and thickness of eutectic Si particles minimizes potential crack initiation sites and delays crack propagation, which has also been reported to enhance ductility [58,59]. Despite exhibiting the finest SDAS, the primary reason for the significant reduction in ductility observed in (BA + HMR-B), compared to the other alloys, is the presence of coarse intermetallic compounds with a volume fraction exceeding 5 %, as shown in Fig. 10(a3) and (b3). These intermetallic act as multiple stress concentration sites under uniaxial tensile loading, which can readily trigger crack initiation at the interfaces between the intermetallic phases and the matrix, ultimately leading to reduced ductility. Although the (BA + HMR-A_2B) contains an approximately 0.43 % higher fraction of intermetallic compounds compared to the BA alloy, this increase is significantly lower than those observed in the (BA + HMR-A) and (BA + HMR-B) (1.04 % and 4 %, respectively), and thus did not critically affect ductility. Overall, the simultaneous refinement of α-Al dendrites, secondary dendrite arm spacing (SDAS), and eutectic Si effectively mitigates the conventional trade-off between strength and ductility, enabling concurrent improvements in both properties.

Fig. 12(c) compares the tensile properties of the HMR alloys with

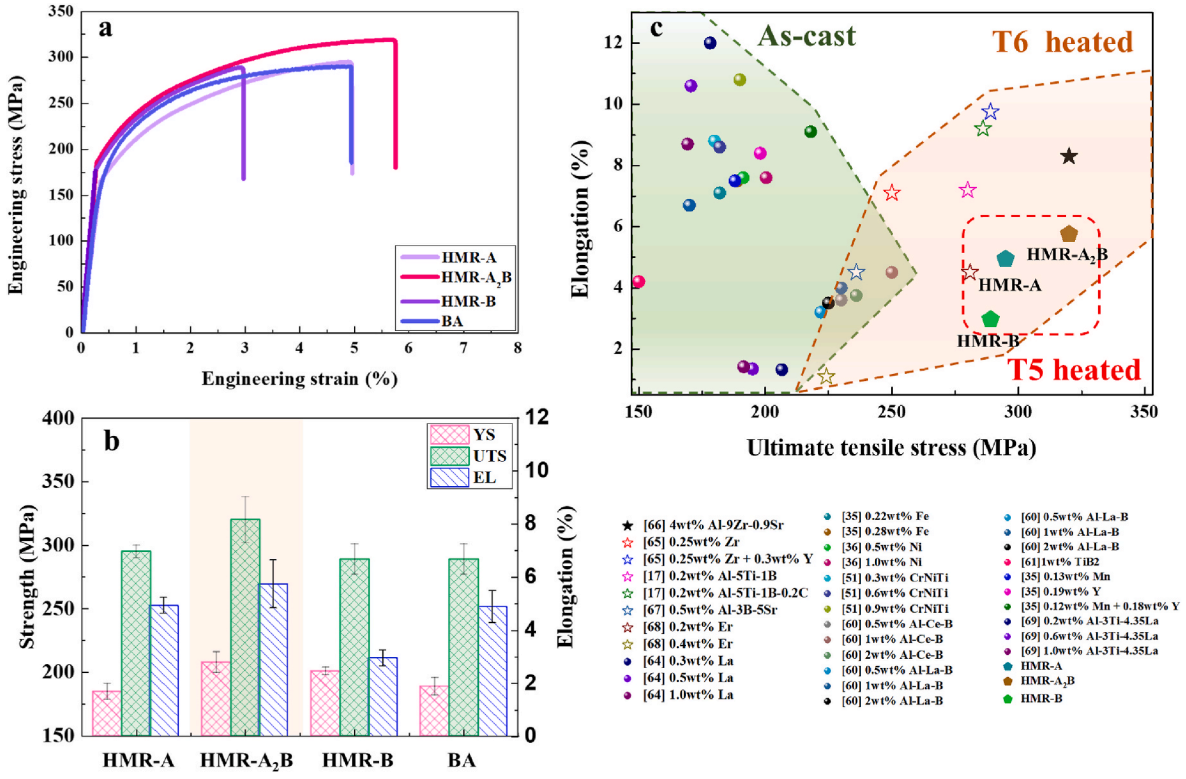

Fig. 12. Comparison of tensile properties in Al alloys adding HMR refiners and previously reported refiners
(a) Engineering stress-strain curves and (b) Uniaxial tensile properties of the (BA + HMR-A), (BA + HMR-A_2B), (BA + HMR-B), and BA (c) Comparison of the tensile properties in as-cast, T6 treated and T5 treated Al alloys adding HMRs and previously reported refiners [17,35,36,51,60,61,64–69]. The T5 treated (BA + HMR-A), (BA + HMR-A_2B), and (BA + HMR-B) in this study represented by pentagon-shaped markers.

those of previously reported refined alloys. The reported refiners were added to Al–7Si wt% and Al–10Si wt% alloys, with circular markers representing the as-cast condition and empty star markers representing T6 heat treatment. (BA + HMR-A), (BA + HMR-A_2B), and (BA + HMR-B) are represented by pentagon-shaped markers. Despite undergoing T5 heat treatment, the alloy developed with (BA + HMR-A_2B) exhibits almost the same strength as the alloy with the Al–9Zr-0.9Sr refiner (black star), which has the highest strength among the refined alloys subjected to T6 heat treatment. However, compared to the Al–9Zr-0.9Sr refiner alloy, the ductility of (BA + HMR-A_2B) appears to be approximately 2.5 % lower, which can be attributed to the difference in heat treatment. Generally, T5 heat treatment omits the solution treatment and quenching process, leaving a coarse microstructure and uneven precipitates formed during casting, which results in lower ductility compared to T6 heat treatment [7,8]. Furthermore, this study focused intensively on the development of a new multifunctional refiner and the analysis of the refinement mechanism; however, there was a lack of investigation into the optimization of the heat treatment and manufacturing process. Thus, the optimization of the heat treatment and manufacturing processes for the developed HMR merits further investigation to achieve significantly superior mechanical properties in Al–Si alloys.

4. Conclusion

In the present study, we successfully developed a novel high-entropy microstructure refiner (HMR) that allows for synergistic multi-phase microstructure refinement of hypoeutectic Al–Si alloys even in T5 heat treatment. We systematically analyzed the microstructure refinement effects and mechanisms according to the HMR compositions and investigated the resulting mechanical properties. Among developed HMR, the HMR-A_2B addition of 0.5 wt% in base alloy (BA) demonstrated the most outstanding synergistic microstructure refinement performance. HMR-A_2B incorporates Group A elements (Ti, Zr, Nb) to promote heterogeneous nucleation, thereby reducing the nucleation undercooling (ΔT_N), as quantitatively validated by DSC in relation to the refinement of α-Al dendrite size. Concurrently, Group B elements (Cr, Fe, Ni) induce constitutional undercooling (ΔT_C) via segregation at the liquid/solid interface, with this segregation behavior experimentally verified through EPMA, providing clear evidence for the underlying ΔT_C driven mechanism. As a result of these effect HMR-A_2B addition in BA leads to significant refinement of α-Al dendrites (89.1 % reduction), secondary dendrite arm spacing (64 % reduction), and eutectic Si spacing (45.95 % reduction), while maintaining minimal precipitation of intermetallic compounds compared to hypoeutectic Al–Si BA. This synergistic multi-phase microstructure refinement allowed for simultaneous 9.1 % increases in yield strength and a 9.6 % improvement in ultimate tensile strength compared to the BA, along with an elongation improvement of 14.8 %. In conclusion, we have developed an HMR with high potential, exhibiting excellent synergistic microstructure refinement performance, which enables simplified refinement processing and simultaneous improvement in both strength and ductility. The simplification of the refinement process is expected to greatly contribute to the development of streamlined post-processes in the industry, which will be directly linked to cost efficiency. Moreover, in the development of T5 heat-treated Al–Si alloys where microstructure control through post-treatment is nearly impossible, the HMR from this study not only demonstrated excellent refinement efficiency but also proved its correlation with mechanical properties. Therefore, the development of this HMR provides a promising guideline for developing high-performance, cost-effective T5-treated Al–Si alloys.

Data availability

The data that support the findings of this study are available from Prof. Park (email: espark@snu.ac.kr) upon reasonable request.

Declaration of competing interest

The authors declare that they have no known competing financial interests or personal relationships that could have appeared to influence the work reported in this paper.

Acknowledgements

This work was supported by the Creative Materials Discovery Program through the National Research Foundation of Korea (NRF) funded by the Ministry of Science and ICT (No. NRF-2019M3D1A1079215 and RS-2023-00281671). In addition, JKK was supported by Industrial Strategy Technology Development Program funded by the Ministry of Trade, Industry & Energy (MOTIE, Korea) (Development of parts integrated technology for rack housing and I-type front subframe for 30 % or more lightweight by high vacuum aluminum diecasting, No. 1415184749). We also acknowledge DESY (Hamburg, Germany), a member of the Helmholtz Association HGF, for the provision of experimental facilities. Parts of this research were carried out at PETRA III. Data was collected using P21.1 beam line operated/provided by DESY Photon Science (or Helmholtz-Zentrum Hereon if applicable). We would like to thank Fernando Igoa and Philipp Glaevecke for assistance during the experiments. Beamtime was allocated for proposal I-20231069.

Appendix A. Supplementary data

Supplementary data to this article can be found online at https://doi.org/10.1016/j.jmrt.2025.08.039.

References

[1] Niu G, Wang Y, Zhu L, Ye J, Mao J. Fluidity of casting Al–Si series alloys for automotive light-weighting: a systematic review. Mater Sci Technol 2022;38(13):902–11.
[2] Hernandez FCR, Ramírez JMH, Mackay R. Al-Si alloys: automotive, aeronautical, and aerospace applications. Springer; 2017.
[3] Kim J, Shin S, Lee S. Correlation between microstructural evolution and corrosion resistance of hypoeutectic al–si–mg alloy: influence of corrosion product layer. Mater Char 2022;193:112276.
[4] Zhang D, Li D, Ren L, Zhao K, Zhao Z, Yan X, Liu G, Cha W, Liu S, Liu X. A new synergy to overcome the strength-ductility trade-off dilemma in al–si–cu alloy by micro-nano-particle complex clusters. Mater Des 2023;230:111973.
[5] Sjölander E, Seifeddine S. The heat treatment of al–si–cu–mg casting alloys. J Mater Process Technol 2010;210(10):1249–59.
[6] Dolan G, Robinson J. Residual stress reduction in 7175-T73, 6061-T6 and 2017A-T4 aluminium alloys using quench factor analysis. J Mater Process Technol 2004;153:346–51.
[7] Fukasawa K, Mohri R, Ohtake T, Inoue T, Kuroda A, Kambe H, Yoshida M. Effect of Mn addition on the age-hardening behavior of an Al-(9–10)% Si-0.3% Mg die casting alloy in T5 and T6 heat treatment. Mater Trans 2016;57(6):959–65.
[8] Kim S-B, Lee J-M, Koo T-M, Lee S-U, Lee J-Y, Son K-S, Cho Y-H. Influence of cooling condition after solidification on T5 heat treatment response of hypoeutectic Al-7Si-0.4 Mg casting alloy. J Alloys Compd 2022;906:164339.
[9] Hu M, Sun D, Zhu M. Simulation of gas porosity formation and interaction with dendrite and eutectic structures during solidification of Al-Si alloys. Mater Des 2024;241:112977.
[10] Xu X, Hao Y, Dong R, Hou H, Zhao Y. Effect of undercooling on microstructure evolution of Cu based alloys. J Alloys Compd 2023;935:167998.
[11] Xu X, Hou H, Zhao Y, Liu F. Nonequilibrium solidification, grain refinements, and recrystallization of deeply undercooled Ni-20 At. Pct Cu alloys: effects of remelting and stress. Metall Mater Trans 2017;48:4777–85.
[12] Xu X, Zhao Y, Hou H, Liu F. Concentration and fluid flow effects on kinetics, dendrite remelting and stress accumulation upon rapid solidification of deeply undercooled alloys. J Alloys Compd 2018;744:740–9.
[13] Xu X, Zhao Y, Hou H. Observation of dendrite growth velocity and microstructure transition in highly undercooled single phase alloys. Mater Char 2019;155:109793.
[14] Sunitha K, Gurusami K. Study of Al-Si alloys grain refinement by inoculation. Mater Today Proc 2021;43:1825–9.
[15] Samuel A, Doty H, Valtierra S, Samuel F. Effect of grain refining and Sr-modification interactions on the impact toughness of al–si–mg cast alloys. Mater Des 2014;56:264–73.
[16] Li P, Liu S, Zhang L, Liu X. Grain refinement of A356 alloy by al–ti–b–c master alloy and its effect on mechanical properties. Mater Des 2013;47:522–8.
[17] Ma S, Wang X. Mechanical properties and fracture of in-situ Al3Ti particulate reinforced A356 composites. Mater Sci Eng, A 2019;754:46–56.

[18] Li D, Zhao K, Liu G, Han M, Liu S, Liu X. Revealing the correlation of microstructure configuration and mechanical properties of Al–Si–Mg alloy reinforced by C-doped TiB2 and SiC. Mater Des 2023;226:111694.
[19] Zhu H, Wang Q, Yang C, Wang Y, Xia C, Zhao D, Zhang H, Wang M, Chen Z, Wang H. Improving TiB2 dispersion in Al-Si composites by interfacial projection: high-throughput first-principles calculations and experimental verification. Mater Des 2024;244:113184.
[20] Zhao Z, Li D, Yan X, Chen Y, Jia Z, Zhang D, Han M, Wang X, Liu G, Liu X. Insights into the dual effects of Ti on the grain refinement and mechanical properties of hypoeutectic Al–Si alloys. J Mater Sci Technol 2024;189:44–59.
[21] Sigworth GK. Grain refinement of Al–Si–Cu alloys by AlB2 and (Al, Ti) B2. Int J Metalcast 2024;18(4):2778–82.
[22] Ibarra G. Control of grain refinement of Al-Si alloys by thermal analysis. 1999.
[23] Zhang M-X, Kelly PM, Easton MA, Taylor JA. Crystallographic study of grain refinement in aluminum alloys using the edge-to-edge matching model. Acta Mater 2005;53(5):1427–38.
[24] Clyne T, Robert M. Stability of intermetallic aluminides in liquid aluminium and implications for grain refinement. Met Technol 1980;7(1):177–85.
[25] Li Y, Hu B, Liu B, Nie A, Gu Q, Wang J, Li Q. Insight into Si poisoning on grain refinement of Al-Si/Al-5Ti-B system. Acta Mater 2020;187:51–65.
[26] Qiu D, Taylor J, Zhang M, Kelly P. A mechanism for the poisoning effect of silicon on the grain refinement of Al–Si alloys. Acta Mater 2007;55(4):1447–56.
[27] Wang F, Qiu D, Liu Z-L, Taylor JA, Easton MA, Zhang M-X. The grain refinement mechanism of cast aluminium by zirconium. Acta Mater 2013;61(15):5636–45.
[28] Li Y, Hu B, Gu Q, Liu B, Li Q. Achievement in grain-refining hypoeutectic Al-Si alloys with Nb. Scr Mater 2019;160:75–80.
[29] Li Y, Jiang Y, Hu B, Li Q. Novel Al-Ti-Nb-B grain refiners with superior efficiency for Al-Si alloys. Scr Mater 2020;187:262–7.
[30] Liu W, Zhang R, Wu X, Li L, Zhang H, Li J, Jiang H. Simulation of grain refinement of Al-8Si-0.2 Mg alloy inoculated with Al-Nb-B via an improved cellular automaton model. Mater Des 2025;249:113561.
[31] Timpel M, Wanderka N, Schlesiger R, Yamamoto T, Lazarev N, Isheim D, Schmitz G, Matsumura S, Banhart J. The role of strontium in modifying aluminium–silicon alloys. Acta Mater 2012;60(9):3920–8.
[32] Ganesh MS, Reghunath N, Levin MJ, Prasad A, Doondi S, Shankar KV. Strontium in Al–Si–Mg alloy: a review. Met Mater Int 2022:1–40.
[33] Yang Y, Zhong S-Y, Chen Z, Wang M, Ma N, Wang H. Effect of Cr content and heat-treatment on the high temperature strength of eutectic Al–Si alloys. J Alloys Compd 2015;647:63–9.
[34] Li Q, Zhu Y, Zhao S, Lan Y, Liu D, Jian G, Zhang Q, Zhou H. Influences of Fe, Mn and Y additions on microstructure and mechanical properties of hypoeutectic Al–7% Si alloy. Intermetallics 2020;120:106768.
[35] Qinglin L, Yan Z, Xiaoyu Z, Chuangzao W, Jianbin Z, Jiqiang M, Xiaowu H, Yefeng L. Influence of Ni and Y plus Ni complex additions on microstructure and mechanical properties of Al–7Si alloy. Int J Metalcast 2022:1–13.
[36] Qinglin L, Shang Z, Xuepeng B, Yushi Z, Yuqian Z, Chuangzao W, Yefeng L, Yuxin Z, Yiandong X. Effects of AlCoCrFeNiTi high-entropy alloy on microstructure and mechanical properties of pure aluminum. J Mater Sci Technol 2020:1–11.
[37] Porter DA, Easterling KE. Phase transformations in metals and alloys (revised reprint). CRC press; 2009.
[38] Taylor JA. The effect of iron in Al-Si casting alloys. In: 35th Australian foundry institute national conference. Adelaide, South Australia: Australian Foundry Institute (AFI); 2004. p. 148–57.
[39] Rohatgi S, Tiwari M, Rathi A, Sharma A. Role of undercooling and effect of solute particles on grain refinement of aluminium alloys. Indian Foundry J 2015;62:31–7.
[40] Xu J, Li Y, Hu B, Jiang Y, Li Q. Development of Al–Nb–B master alloy with high Nb/B ratio for grain refinement of hypoeutectic Al–Si cast alloys. J Mater Sci 2019;54:14561–76.
[41] Easton M, StJohn D. An analysis of the relationship between grain size, solute content, and the potency and number density of nucleant particles. Metall Mater Trans 2005;36(7):1911–20.
[42] Maxwell I, Hellawell A. A simple model for grain refinement during solidification. Acta Metall 1975;23(2):229–37.
[43] Ponsoni JB, Aranda V, da Silva Nascimento T, Strozi RB, Botta WJ, Zepon G. Design of multicomponent alloys with C14 laves phase structure for hydrogen storage assisted by computational thermodynamic. Acta Mater 2022;240:118317.
[44] Dash S, Li D, Zeng X, Chen D. Heterogeneous microstructure and deformation behavior of an automotive grade aluminum alloy. J Alloys Compd 2021;870:159413.
[45] Easton M, Qian M, Prasad A, StJohn D. Recent advances in grain refinement of light metals and alloys. Curr Opin Solid State Mater Sci 2016;20(1):13–24.
[46] Höhne GWH, Hemminger W, Flammersheim H-J. Differential scanning calorimetry. Springer; 2003.
[47] Ferreira EB, Lima ML, Zanotto ED. DSC method for determining the liquidus temperature of glass-forming systems. J Am Ceram Soc 2010;93(11):3757–63.
[48] Schmid-Fetzer R, Kozlov A. Thermodynamic aspects of grain growth restriction in multicomponent alloy solidification. Acta Mater 2011;59(15):6133–44.
[49] Vandersluis E, Ravindran C. Comparison of measurement methods for secondary dendrite arm spacing. Metallogr Microstruct Anal 2017;6:89–94.
[50] Easton M, Davidson C, St John D. Effect of alloy composition on the dendrite arm spacing of multicomponent aluminum alloys. Metall Mater Trans 2010;41:1528–38.
[51] Zhang J, Qiao Z, Li Q, Wang K, Ma J, Lan Y. Effects of new grain refiner AlCrNiTi on the microstructure and mechanical properties of Al–7Si-Based alloy. Int J Metalcast 2024;18(1):445–56.
[52] Sivarupan T, Caceres CH, Taylor JA. Alloy composition and dendrite arm spacing in Al-Si-Cu-Mg-Fe alloys. Metall Mater Trans 2013;44:4071–80.
[53] Li Q, Zhao S, Li B, Zhu Y, Wang C, Lan Y, Xia T. A novel modifier on the microstructure and mechanical properties of Al-7Si alloys. Mater Lett 2019;251:156–60.
[54] Li Q, Zhang Y, Zhang X, Zhao S, Lan Y, Xia T, Hu X. Microstructure evolution and nano-phases strengthening of Al-5% Cu alloy by adding trace AlSiTiCrNiCu high entropy alloy. Mater Char 2021;175:111100.
[55] Yajjala RK, Inampudi NM, Jinugu BR. Correlation between SDAS and mechanical properties of Al–Si alloy made in sand and slag moulds. J Mater Res Technol 2020;9(3):6257–67.
[56] Koutiri I, Bellett D, Morel F, Augustins L, Adrien J. High cycle fatigue damage mechanisms in cast aluminium subject to complex loads. Int J Fatig 2013;47:44–57.
[57] Houria MI, Nadot Y, Fathallah R, Roy M, Maijer DM. Influence of casting defect and SDAS on the multiaxial fatigue behaviour of A356-T6 alloy including mean stress effect. Int J Fatig 2015;80:90–102.
[58] Jiang B, Ji Z, Hu M, Xu H, Xu S. A novel modifier on eutectic Si and mechanical properties of Al-Si alloy. Mater Lett 2019;239:13–6.
[59] Zheng Q, Zhang L, Jiang H, Zhao J, He J. Effect mechanisms of micro-alloying element La on microstructure and mechanical properties of hypoeutectic Al-Si alloys. J Mater Sci Technol 2020;47:142–51.
[60] Jing L, Pan Y, Lu T, Chai W. Refinement effect of two rare earth borides in an Al-7Si-4Cu alloy: a comparative study. Mater Char 2018;145:664–70.
[61] Wang T, Chen Z, Zheng Y, Zhao Y, Kang H, Gao L. Development of TiB2 reinforced aluminum foundry alloy based in situ composites–Part II: enhancing the practical aluminum foundry alloys using the improved Al–5 wt% TiB2 master composite upon dilution. Mater Sci Eng, A 2014;605:22–32.
[62] Ahmad R, Asmael M. Influence of cerium on microstructure and solidification of eutectic Al–Si piston alloy. Mater Manuf Process 2016;31(15):1948–57.
[63] Tahiri H, Mohamed S, Doty H, Valtierra S, Samuel F. Effect of Sr–grain refining–Si interactions on the microstructural characteristics of Al–Si hypoeutectic alloys. Int J Metalcast 2018;12(2):343–61.
[64] Ahmad R, Asmael M. Influence of lanthanum on solidification, microstructure, and mechanical properties of eutectic Al-Si piston alloy. J Mater Eng Perform 2016;25:2799–813.
[65] Fang X, Zhang T, Dong B, Yuan Z, Huang Z, Yan F, Zu F. Simultaneous refinement of α-Al and modification of Si in Al–Si alloy achieved via the addition of Y and Zr. J Mater Res Technol 2024;30:1822–33.
[66] Ding J, Lu C, Sun Y, Cui C, Zhao E. Refining and modification effects of (Al, Zr, Si)–Al4Sr on Al–7Si–0.5 Mg alloy. J Mater Res Technol 2021;15:1604–12.
[67] Cui X, Wu Y, Gao T, Liu X. Preparation of a novel Al–3B–5Sr master alloy and its modification and refinement performance on A356 alloy. J Alloys Compd 2014;615:906–11.
[68] Colombo M, Gariboldi E, Morri A. Er addition to Al-Si-Mg-based casting alloy: effects on microstructure, room and high temperature mechanical properties. J Alloys Compd 2017;708:1234–44.
[69] Ding W, Gou L, Hu L, Zhang H, Zhao W, Ma J, Qiao J, Li X. Modification of eutectic Si in hypoeutectic Al-Si alloy with novel Al-3Ti-4.35 La master alloy. J Alloys Compd 2022;929:167350.